

BACHELOR THESIS

BIOMEDICAL ENGINEERING



Universidad
Carlos III de Madrid



Universidad
Rey Juan Carlos

PARTIAL VOLUME CORRECTION FOR ARTERIAL SPIN LABELING SEQUENCES IN MAGNETIC RESONANCE IMAGING. 3DSLICER EXTENSION

AUTHOR

Miguel López Gavilán

TUTORS

Javier Pascau González-Garzón (UC3M)

Pablo García-Polo García (URJC)

Norberto Malpica González de Vega (URJC)

A mis tutores, por su tiempo e implicación, esenciales para la realización de este proyecto;

A mi familia y amigos, por su inestimable apoyo y compañía,

Muchas gracias

ABSTRACT

Arterial spin labeling is becoming an increasingly popular method for evaluating the cerebral blood flow. However, one of the major limitations of arterial spin labeling (and other perfusion assessment methods like PET) is the partial volume effect, by which each voxel of the image contains a mixture of tissues due to the low spatial resolution of ASL. Partial volume correction is required to retrieve the perfusion contribution of each of these tissues, which is important in the study of neurodegenerative diseases such as Alzheimer's disease.

A new partial volume correction method (3D weighted least squares) based on an existing state-of-the-art method (Asllani's algorithm) is presented in this work. The new algorithm improves the previous algorithm by operating in a 3D way instead of a 2D way and including a weighting to the regression problem as a function of the distance between the voxels. The new method was tested over simulated cerebral perfusion images, giving better results than the Asllani's algorithm.

The algorithm was also implemented as a graphical user interface extension for the open source platform 3DSlicer. This extension automates all the correction process and allows the researchers processing the ASL images rapidly and easily.

Using this extension, a real perfusion study was conducted to compare the cerebral perfusion between Alzheimer and control groups in resting state. Alzheimer group showed a significantly lower perfusion in the thalamus, caudate nucleus, hippocampus and cuneus. These regions have been reported in the literature to present atrophies in Alzheimer subjects and are involved in cognitive functions that are negatively affected by the disease. These results provide further validation for the 3DWLS as a suitable correction method and for the extension as a useful research tool.

ACRONYMS

2D – two dimensional	GUI – graphical user interface
3D – three dimensional	Hb – hemoglobin
3DWLS – 3D weighted least squares	IR – inversion recovery
AD – Alzheimer’s disease	LUT – look up table
ASL – arterial spin labeling	MCR – matlab compiler runtime
ATP – adenosine triphosphate	MNR – magnetic nuclear resonance
BOLD – blood oxygen level dependent	MRI – magnetic resonance imaging
BW – bandwidth	PASL – pulsed arterial spin labeling
CASL – continuous arterial spin labeling	pCASL – pseudo continuous arterial spin labeling
CFB – cerebral blood flow	PET – positron emission tomography
CSF – cerebrospinal fluid	PULSAR - pulsed star labeling of arterial regions
CT – computed tomography	PVC – partial volume correction
dHb – deoxyhemoglobin	PVE – partial volume effect
EPI – echo planar imaging	RF – radiofrequency
EPISTAR – echo planar imaging and signal targeting with alternating radiofrequency	RMSE – root mean square error
FA – fractional aniso-probability	SE – spin echo
FAIR – flow-sensitive alternating inversion recovery	SNR – signal to noise ratio
FID – free induction decay	SPECT – single photon emission computed tomography
fMRI – functional magnetic resonance imaging	SPM – statistical parametric mapping
FT – Fourier transform	TE – echo time
FWHM – full width at half maximum	TI – inversion time
GM – grey matter	TR – repetition time
GRE – gradient echo	WM – white matter

Table of contents

CHAPTER 1: Introduction	- 1 -
1.1 Motivation.....	- 1 -
1.2 Objectives	- 2 -
1.3 Background on MRI.....	- 3 -
Physical principles.....	- 3 -
Signal generation	- 5 -
Spatial encoding	- 8 -
Image reconstruction	- 10 -
Pulse sequences.....	- 11 -
Advantages and disadvantages of MRI	- 13 -
1.4 Cerebral perfusion imaging	- 15 -
PET	- 15 -
BOLD fMRI	- 15 -
ASL	- 16 -
Comparison between imaging methods	- 19 -
1.4 The partial volume effect problem in ASL imaging	- 20 -
1.5 State of the art.....	- 22 -
PET legacy algorithm	- 22 -
Asllani regression algorithm	- 23 -
CHAPTER 2: 3DWLS algorithm for PVC	- 27 -
2.1 Algorithm description	- 27 -
2.2 Algorithm evaluation	- 33 -
Materials.....	- 33 -
Methods.....	- 38 -
Results.....	- 39 -
Discussion	- 43 -
2.3 3DWLS flowchart	- 45 -
CHAPTER 3: 3D Slicer extension	- 47 -
3.1 Extension dependencies.....	- 47 -
3.2 Features description	- 48 -

Importation and visualization of ASL and anatomical images.	- 48 -
Image spatial processing	- 49 -
Alternative coregistration.....	- 50 -
Independent PVC per brain regions	- 51 -
Regression kernel size and weighting type selection.....	- 52 -
Normalization and smoothing of PVC results.....	- 52 -
Exportation and visualization of PVC results.....	- 53 -
3.3 Extension workflow diagram	- 55 -
CHAPTER 4: Comparison of cerebral perfusion in Alzheimer’s disease.....	- 57 -
4.1 Brief overview of Alzheimer’s disease.....	- 57 -
4.2 Subjects and methods	- 57 -
4.3 Results and discussion	- 60 -
Perfusion comparison without PVC.....	- 62 -
CONCLUSION AND FUTURE WORK.....	- 64 -
SOCIO-ECONOMIC FRAMEWORK	- 66 -
REGULATORY FRAMEWORK	- 67 -
Bibliography.....	- 69 -

List of figures

Fig. 1.1 nucleus magnetic moment precession[36].....	- 3 -
Fig. 1.2 nuclei spin alignment in the presence of a magnetic field[37][42]	- 4 -
Fig. 1.3 magnetization vector precession after applying the RF pulse[39]	- 5 -
Fig. 1.4 T1 & T2 relaxation processes (fat).....	- 6 -
Fig. 1.5 T1 difference between tissues and contrast.....	- 7 -
Fig. 1.6 FID signal and echo decay along time	- 8 -
Fig. 1.7 effect of the gradient slope and RF pulse BW in the slice thickness	- 9 -
Fig. 1.8 k-space of a slice(left). Ordered k-space matrix rows around the central echo (right). ...	- 10 -
Fig. 1.9 basic spin echo acquisition scheme[40].....	- 11 -
Fig. 1.10 TR and TE effect in MRI contrast[41].....	- 12 -
Fig. 1.11 inversion areas (red) in FAIR-MRI during slice (green) acquisition[42]	- 18 -
Fig. 1.12 EPSTAR slice acquisition[42].....	- 19 -
Fig. 1.13 ASL and anatomical MRI resolution comparison.....	- 20 -
Fig. 1.14 spatial preprocessing step before PVC (coregistration & segmentation)	- 24 -
Fig. 1.15 RMSE value vs regression kernel size[20].....	- 25 -
Fig. 2.1 3x3x3 distance matrix [D].....	- 28 -
Fig. 2.2 5x5x1 distance matrix [D].....	- 28 -
Fig. 2.3 3D plot of 5x5x3 distance weighting kernel(interpolated)	- 29 -
Fig. 2.4 5x5x3 distance weighting kernel values	- 29 -
Fig. 2.5 3D plot of 5x5x3 exponential weighting kernel(interp.)	- 30 -
Fig. 2.6 5x5x3 exponential weighting kernel values.....	- 30 -
Fig. 2.7 3D plot of 5x5x3 Gaussian weighting kernel(interp.)	- 31 -
Fig. 2.8 5x5x3 Gaussian weighting kernel values.....	- 31 -
Fig. 2.9 normal random noise for simulated CBF maps	- 35 -
Fig. 2.10 Artf. GM perfusion (Type 1).....	- 35 -
Fig. 2.11 Artf. WM perfusion (Type 1).....	- 35 -
Fig. 2.12 Artf. CSF perfusion (Type 1).....	- 35 -
Fig. 2.13 Artf. ASL image (Type 1).....	- 35 -
Fig. 2.14 sinusoidal noise for type 2 artificial CBF map generation	- 36 -
Fig. 2.15 Artf. GM perfusion (Type 2).....	- 37 -
Fig. 2.16 Artf. WM perfusion (Type 2).....	- 37 -
Fig. 2.17 Artf. CSF perfusion (Type 2).....	- 37 -
Fig. 2.18 Artf. ASL image (Type 2).....	- 37 -
Fig. 2.19 Atrophy 1. two overlapping hypoperfusion regions in GM	- 38 -
Fig. 2.20 Atrophy 2. two overlapping hypoperfusion and hyperperfusion regions in GM	- 38 -
Fig. 2.21 Atrophy 3. two non-overlapping hypoperfusion and hyperperfusion regions in GM	- 38 -
Fig. 2.22 Atrophy 4: GM hypoperfusion atrophy overlapping a WM hyperperfusion atrophy	- 38 -
Fig. 2.23 Atrophy 5: two non-overlapping hypoperfusion and hyperperfusion regions in WM.....	- 38 -
Fig. 2.24 RMSE values using distance weighting and FA	- 39 -
Fig. 2.25 RMSE values using exponential weighting and FA	- 39 -
Fig. 2.26 RMSE values using Gaussian weighting and FA	- 39 -
Fig. 2.27 RMSE values using distance weighting	- 40 -
Fig. 2.28 RMSE values using exponential weighting	- 40 -
Fig. 2.29 RMSE values using Gaussian weighting	- 40 -
Fig. 2.30 RMSE values using FA.....	- 40 -

Fig. 2.31 RMSE values using Asllani's algorithm	- 40 -
Fig. 2.32 RMSE values on atrophies using distance weighting and FA	- 41 -
Fig. 2.33 RMSE values on atrophies using exponential weighting and FA	- 41 -
Fig. 2.34 RMSE values on atrophies using Gaussian weighting and FA	- 41 -
Fig. 2.35 RMSE values on atrophies using distance weighting	- 42 -
Fig. 2.36 RMSE values on atrophies using exponential weighting	- 42 -
Fig. 2.37 RMSE values on atrophies using Gaussian weighting	- 42 -
Fig. 2.38 RMSE values on atrophies using FA	- 42 -
Fig. 2.39 RMSE values on atrophies using Asllani's algorithm	- 42 -
Fig. 2.40 RMSE values 2D vs 3D using distance weighting	- 43 -
Fig. 2.41 RMSE values 2D vs 3D using exponential weighting	- 43 -
Fig. 2.42 RMSE values 2D vs 3D using Gaussian weighting	- 43 -
Fig. 3.1 complete view of the 3DSlicer extension GUI	- 48 -
Fig. 3.2 image importation widget and example	- 49 -
Fig. 3.3 alternative image importation widget	- 50 -
Fig. 3.4 T1 image (sagittal slice)	- 50 -
Fig. 3.5 ASL image (sagittal slice)	- 50 -
Fig. 3.6 PD image (sagittal slice)	- 50 -
Fig. 3.7 label image and LUT importation widget	- 51 -
Fig. 3.8 label image displayed over a T1 anatomical image	- 51 -
Fig. 3.9 kernel size and weighting type selection widgets	- 52 -
Fig. 3.10 normalization and smoothing widgets	- 53 -
Fig. 3.11 example of normalized output	- 53 -
Fig. 3.12 output folder selector widget	- 54 -
Fig. 4.1 slices from the average ASL image of one subject of the study	- 58 -
Fig. 4.2 slices from the corrected GM perfusion of one subject of the study	- 59 -
Fig. 4.3 slices from the corrected WM perfusion of one subject of the study	- 59 -
Fig. 4.4 statistic results (Control > Alzheimer), GM perfusion	- 60 -
Fig. 4.5 statistic results (Control > Alzheimer), WM perfusion	- 60 -
Fig. 4.6 statistic results (Alzheimer > Control), WM perfusion	- 60 -
Fig. 4.7 statistic results (Control > Alzheimer), original ASL	- 62 -
Fig. 4.8 statistic results (Alzheimer > Control), original ASL	- 62 -

CHAPTER 1: Introduction

1.1 Motivation

Arterial spin labeling (ASL) is a magnetic resonance imaging (MRI) technique that allows obtaining quantitative 3D maps of the blood flow -also known as perfusion- irrigating the tissues, non-invasively and without requiring any exogenous contrast. The intensity values of those maps or images represent a measurement (commonly expressed as ml/100g/min) of the microvasculature in those tissues. This technique is extensively used for obtaining cerebral perfusion maps, and it is applied in a wide variety of pathologies such as ictus, cancer, epilepsy and neurodegenerative diseases such as the Alzheimer's disease (AD).

Some studies relative to AD have reported a decrease in perfusion at key regions of the brain. The hypothesis suggests that this localized hypoperfusion appears prior to the manifestation of the first signs of tissue atrophy [1]. Therefore, it is paramount to obtain quantitative perfusion maps for each of the brain tissue types, i.e. grey matter (GM), white matter (WM) and cerebrospinal fluid (CSF), in order to validate such hypothesis.

However, one of the main disadvantages of ASL is the partial volume effect (PVE) at voxel level. In order to have a suitable signal-to-noise ratio and reliable quantitative perfusion maps, the imaging process trades off spatial resolution, with a resulting voxel size around $3 \times 3 \times 6 \text{ mm}^3$. This makes the voxels of the image often to contain a mixture of GM, WM and CSF, which have different average perfusion values [2]. Partial volume correction (PVC) is therefore necessary to retrieve the individual perfusion information relative to each of the tissues. Currently, some algorithms exist for PVC but they operate at slice (2D) level without incorporating the additional information present in the upper and lower slices and in the neighbor voxels.

The assessment of hypoperfused areas through partial volume corrected ASL images could become a useful clinical tool to provide an early diagnosis of some neurodegenerative diseases. While the clinical evaluation of dementia or cognitive impairment is relatively easy, the causes beneath those symptoms could be diverse and are not that easy to determine. Often, AD is diagnosed at advanced stages of the disease, at which the brain damage is clearly noticeable and irreversible. An early diagnosis will be very positive in terms of prevention and treatment of such neurodegenerative diseases, which translates into a better quality of life for the patient and their relatives.

1.2 Objectives

This bachelor thesis comprises **five objectives**:

1. Gather a deep understanding about MRI, the ASL technique and the existing state-of-the-art methods for PVC of ASL images through bibliographic revision.(CHAPTER 1)
2. Implementation of a new algorithm (3DWLS) for PVC, based on one of the mentioned state-of-the-art methods (Asllani's algorithm).(CHAPTER 2)
3. Evaluation of the 3DWLS algorithm over simulated cerebral perfusion images. (CHAPTER 2)
4. Development of a GUI extension for the platform 3DSlicer that integrates the 3DWLS algorithm, together with the standard pipeline for functional brain image processing.(CHAPTER 3)
5. Carry out a brain perfusion study between Alzheimer and control groups, using the created extension and algorithm implementation.(CHAPTER 4)

1.3 Background on MRI

Magnetic resonance imaging (MRI) is currently an extensively used medical image modality because it allows obtaining both high quality anatomical and functional volumetric images of the body.

Physical principles

Image acquisition is based on the physical principle of magnetic nuclear resonance (MNR) by which the nuclei of certain atoms are able to absorb and re-emit electromagnetic radiation in the presence of a strong magnetic field.

Elementary particles experiment a permanent angular momentum around some axis, also known as spin. Spin can be of + or – orientation and particles with opposite spin sign can couple to cancel out the net observable spin. The net spin of a nucleus is determined by the spin of its particles. Because spin cancellation occurs between pairs of particles, only nuclei having an odd number of protons and neutrons possess an associated net spin or angular momentum. Any rotating charge produces a magnetic moment so these nuclei have also an associated magnetic moment $\vec{\mu}$ related to their spin. The relationship between the magnetic moment and the angular momentum \vec{L} is defined by the gyromagnetic constant γ , which is specific for each element:

$$\gamma = \frac{|\vec{\mu}|}{|\vec{L}|} \quad (1)$$

In natural conditions, the magnetic moment of the nuclei point in random orientation. However, in the presence of a strong magnetic field, the magnetic moment experiments a precession around the field direction. The precession frequency, also known as Larmor frequency ω_0 , depends on γ and the intensity of the magnetic field B_0 , as described by the Larmor equation [3]:

$$\omega_0 = \gamma \cdot B_0 \quad (2)$$

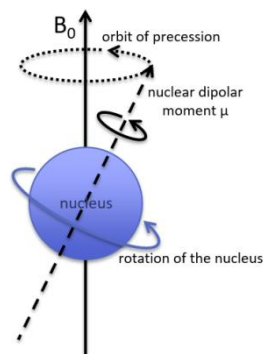


Fig. 1.1 nucleus magnetic moment precession[36]

As stated by the Larmor equation, the precession frequency increases proportionally to the intensity of the external magnetic field.

In the presence of an external magnetic field, the different spin orientations have different associated energies. In the case of the hydrogen atom, spin orientation can be parallel (up) or anti-parallel (down), being the lower and higher energy levels respectively. The energy difference between those states is defined by the following equation:

$$\Delta E = \hbar \cdot \gamma \cdot B_0 \quad (3)$$

\hbar : reduced Plank's constant

At room temperature, the number of parallel spin nuclei is slightly higher than the number of anti-parallel spin nuclei. Although the nuclei flip the spin states continuously, the up/down ratio remains constant (dynamic equilibrium) if no other external influence is introduced. This ratio is governed by the statistical law of Maxwell-Boltzmann [4]:

$$\frac{N_{up}}{N_{down}} = e^{\Delta E/kT} \quad (4)$$

k : Boltzmann's constant

T : temperature (in Kelvin)

Due to the spin alignment towards the field direction and the up/down difference, a net magnetization vector \vec{M} arises from the summation of all individual spins. The net magnetization vector is low in magnitude and has only a longitudinal component M_z that points in the direction of the field. Transversal component M_{xy} contributions cancel out.

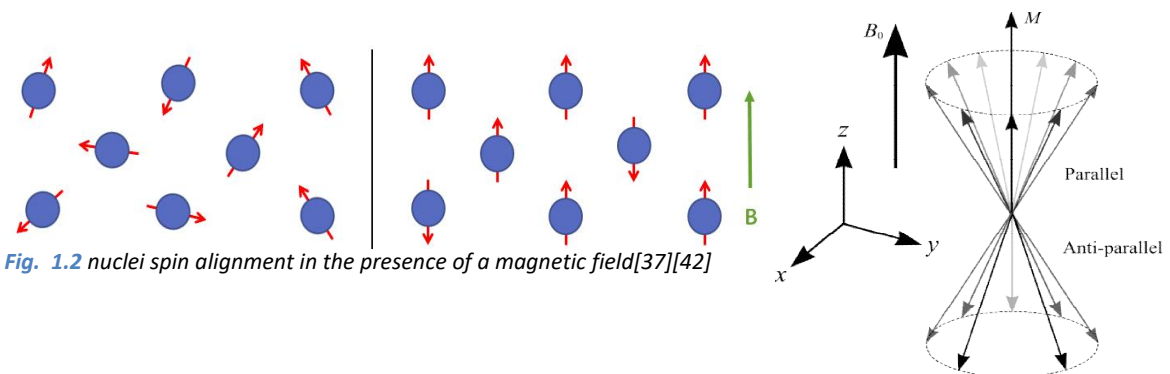


Fig. 1.2 nuclei spin alignment in the presence of a magnetic field[37][42]

$$\vec{M} = \sum_{n=1}^{Ns} \vec{\mu}_n \quad (5)$$

Signal generation

In the presence of a static magnetic field, the magnetization vector remains at equilibrium pointing towards the direction of the field (z axis). In order to produce a measurable signal, this equilibrium is disturbed by applying a radiofrequency (RF) pulse orthogonally to the main magnetic field and exploiting the magnetic resonance phenomenon.

During the application of the RF pulse, the nuclei of the sample absorb energy if the resonance condition is met. The resonance condition states that this absorption occurs if the energy supplied is the same that the energy difference between the spin states i.e., if the frequency of the RF pulse matches the Larmor frequency of the nuclear spin system. If a suitable pulse is applied, the magnetization vector will experiment a precession around the main field direction at a frequency equal to the Larmor frequency, following a spiral-like trajectory (a) and losing longitudinal component in favor of transversal component. If we depict this process using a rotating frame of reference (b) the magnetization follows a tilt-down movement towards the horizontal (xy) axis [5].

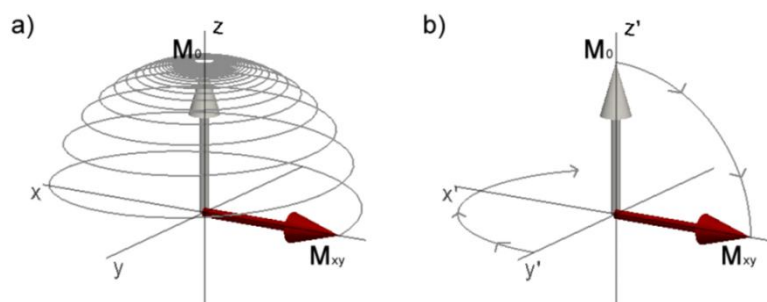


Fig.1.3 magnetization vector precession after applying the RF pulse[39]

The tilt-down angle with respect the field axis is called the flip angle and depends on the duration of the RF pulse:

$$\alpha = \gamma \cdot B_1 \cdot t_p \quad (6)$$

B₁:RF pulse intensity

t_p: pulse duration

When the RF pulse finishes, the magnetization vector returns the previous equilibrium state, progressively realigning with the main magnetic field. This realignment is the result of two independent relaxation processes [5]:

-Longitudinal (T_1) relaxation consists in an energy transfer between the excited nuclei and the surrounding molecular lattice. This distribution of energy returns the longitudinal magnetization component M_z back to the equilibrium state. M_z recovers its equilibrium following an exponential fashion:

$$M_z(t) = M_0(1 - e^{-t/T_1}) \quad (7)$$

M_0 : M_z magnitude at equilibrium

t : time

T_1 : time at which $M_z(t) = 63\%$ of M_0

-Transverse (T_2) relaxation consists in an energy transfer between nuclei. When the RF pulse is removed, phase incoherence in the precession of the nuclei gradually increases. During this process, the transversal magnetization component M_{xy} is progressively disappears. M_{xy} decays from its initial value following an inverse exponential factor:

$$M_{xy}(t) = M_{xy}(0) \cdot e^{-t/T_2} \quad (8)$$

$M_{xy}(0)$: M_{xy} initial value

t : time

T_2 : time at which $M_{xy}(t) = 37\%$ of $M_{xy}(0)$

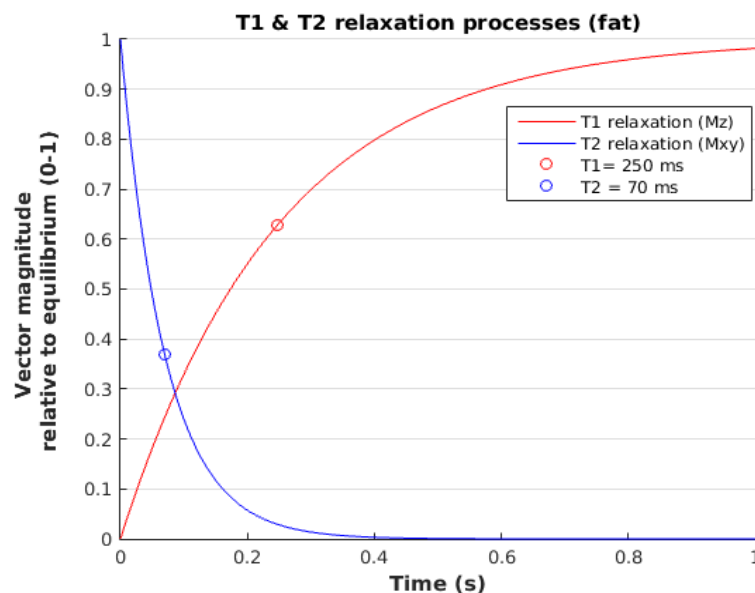


Fig. 1.4 T1 & T2 relaxation processes (fat)

Each tissue has a characteristic T1 and T2 relaxation times. This difference in relaxation times can be exploited to produce T1 or T2 weighted images that increase the contrast between target tissues in the image. This contrast arises from the difference in signal

amplitude contribution coming for each of those tissues at a suitable measurement time.

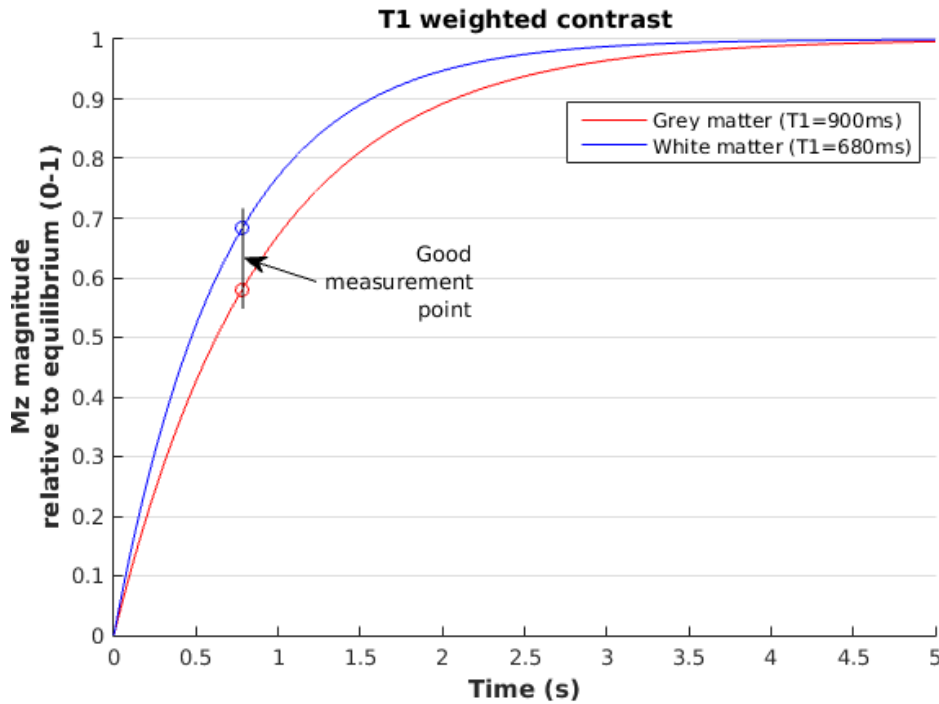


Fig. 1.5 T1 difference between tissues and contrast

The spin coherence is also affected by the inhomogeneities present in the main magnetic field. T_2^* relaxation time accounts for both dephasing effects (T_2 relaxation phase incoherence + magnetic field inhomogeneities)

$$\frac{1}{T_2^*} = \frac{1}{T_2} + \frac{1}{T_{2_{inhom}}} \quad (9)$$

The change in the magnetization vector direction during the relaxation processes back to the initial equilibrium direction induces an electric current in a coil, which represents the measured signal. This free induction decay (FID) signal consists in a short-lived sinusoidal wave that oscillates at the Larmor frequency and whose initial amplitude, that is proportional to the density of the observed excited nuclei, decays exponentially with a time constant of T_2^* [7].

The signal strength is also influenced by the flip angle:

$\alpha = 90^\circ$ -> maximum signal intensity

$\alpha < 90^\circ$ -> weaker signal, faster acquisition (shorter excitation and relaxation)

$\alpha > 90^\circ$ -> weaker signal, slower acquisition, longer relaxation processes

When the RF pulse is stopped, dephasing starts. If we apply a 180° pulse after the dephasing, we will reverse the effect of the field inhomogeneities. The relaxation after the 180° pulse has not a dephasing but a rephasing effect: spins rejoin together in the opposite horizontal direction and start separating again after the rephasing. This generates an echo, which is measured in the coil from the moment the phases are rejoining (relaxation after the 180° pulse) to the moment they are totally dephased again.

The maximum amplitude between the initial FID signal and the echo shows a T_2 decay

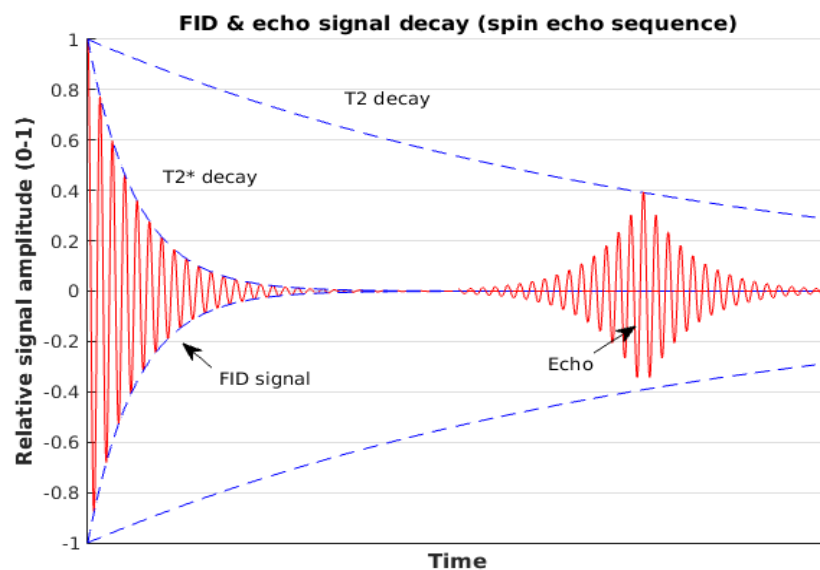


Fig. 1.6 FID signal and echo decay along time

Spatial encoding

Because the main magnetic field is static, all nuclei of the same specie will precess at the same Larmor frequency. Therefore, if an RF pulse of that Larmor frequency is applied only under these conditions, the measured signal would arise from all excited nuclei in the body and it will be impossible to discriminate the signal contributions of local nuclei densities at each region of the space

To retrieve the spatial information, three additional weak magnetic fields (z,x,y gradients) are added to the main magnetic field to distribute the Larmor frequencies attained by such nuclei in a linear predictable pattern, depending on the position. These gradients are generated by three orthogonal gradient coils.[8]

- **Slice selection**

If a gradient is applied along one direction \vec{D}_1 at the same time of emitting the RF excitation pulse, only the perpendicular slice to \vec{D}_1 having a Larmor frequency equal to the pulse frequency will be excited, while the other regions remain unaffected due to

frequency mismatch. Slice selection can be made in any direction, including oblique directions by turning two gradient coils at the same time.

The slice thickness is determined by the bandwidth (BW) of the RF pulse and the slope of the gradient. By emitting an RF pulse with a certain frequency BW, all locations with Larmor frequency within that range will be excited by the RF pulse. Thus, the wider the BW, the thicker the slice.

If the slope of the gradient is increased, the range of Larmor frequencies matching the BW of the pulse will be located at a narrower region of the body. Thus, the stronger the gradient, the thinner the slice.

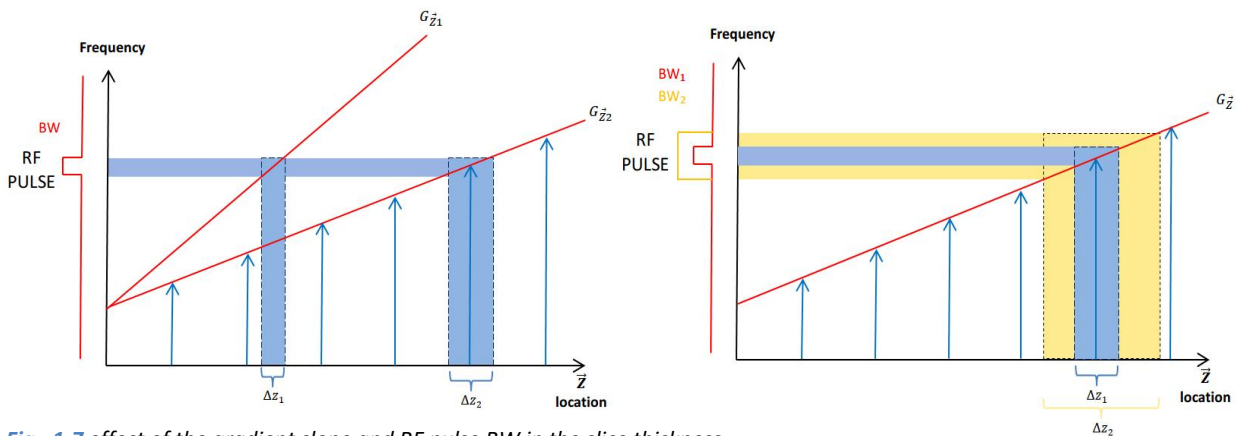


Fig. 1.7 effect of the gradient slope and RF pulse BW in the slice thickness

- **Phase encoding**

After the selection of the slice, another gradient is applied along a perpendicular direction \vec{D}_2 , making the spins to precess at different Larmor frequencies depending on the location in the selected slice along \vec{D}_2 . As a result, magnetic moment vectors dephase as they are precessing at different speeds. When the gradient is shut down, all the spins return to precess at the same frequency but keeping the phase shift.

As the location of a spin is further from the slice center along \vec{D}_2 , this phase shift is higher because the precessing frequency difference with respect the initial Larmor frequency is progressively larger. In turn, at the central location, $B = B_0$, so there is no phase shift at that location.

By increasing or decreasing the strength of the gradient, the induced phase differences will be higher or lower respectively. If different (slope) gradients are applied each time a new echo is measured, each signal sample will correspond to the same whole column (along \vec{D}_2) of the selected slice in all echoes but the amplitudes at those points will be different depending on the effect of the different phase shifting. By comparing these differences in amplitude between equivalent points in the measured echoes, the individual contributions along \vec{D}_2 can be obtained.

- **Frequency encoding**

The frequency encoding gradient is applied along the remaining orthogonal direction \vec{D}_3 during the sampling of the echo, after the slice selection and phase encoding gradients. By means of this last gradient, all spins within the slice will precess at different predictable Larmor frequencies depending on their location along \vec{D}_3 . The signal measured in the coil is the summation of the contributions of individual spins, thus being composed of varying amplitude and frequency components.

Because the addition of the multiple sinusoidal signals of different frequencies and amplitudes is equivalent to an inverse Fourier transform, the individual components can be obtained by applying a Fourier transform (FT).

Image reconstruction

The grid of raw data obtained directly from the MR signal echoes is called the K-space. During acquisition, the phase encoding gradient slope is decreasingly changed from a maximum positive slope to a maximum negative slope. The classical method for constructing the k-space matrix is by placing each of the obtained echoes as the corresponding line following the previous order of acquisition. There are other more modern methods that fill the k-space radially or in spiral.

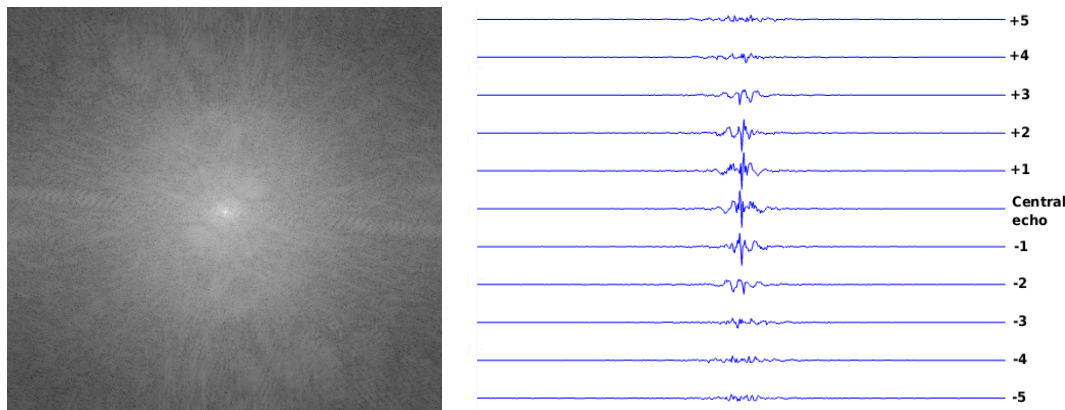


Fig. 1.8 k-space of a slice(left). Ordered k-space matrix rows around the central echo (right).

If the FT is applied to each echo (i.e. along each row of the k-space) the frequency-encoded spatial information is obtained. If we apply the FT along the columns, the phase-encoded spatial information is obtained. Therefore, the k-space is equivalent to the 2D inverse Fourier transform of the slice image which can be reconstructed by applying a 2D FT.

The spatial resolution over \vec{D}_1 depends on the bandwidth of the RF pulse and the slope of the slice selection gradient.

The spatial resolution over \vec{D}_2 depends on the number of echoes recorded at different phase encoding gradient slopes.

The spatial resolution over \vec{D}_3 depends on the number of samples measured for each echo, i.e. it depends on the sampling rate of the analog-to-digital converter.

Pulse sequences

A pulse sequence is an ordered combination of RF pulses and magnetic field gradients designed to acquire the data to form the image. The number, type, order and duration of the RF pulses and field gradients determine each pulse sequence and image application. [9]

The basic acquisition scheme is depicted in the following figure:

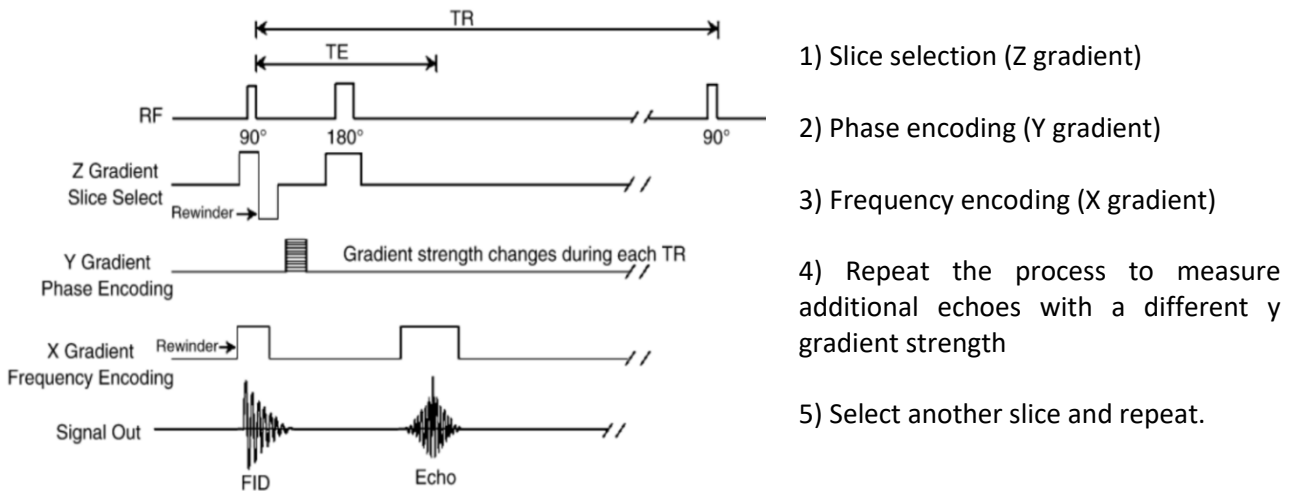


Fig. 1.9 basic spin echo acquisition scheme[40]

TE (echo time) is the time between two consecutive echoes and it is determined by the time interval between the end of the excitation pulse and the emission of the rephasing pulse. This interval is equal to $TE/2$.

The maximum intensity of the echoes decays as T_2 , and this T_2 value is different between tissues. If the TE is extended out over a very long time, only tissues with a very long T_2 relaxation time will retain a significant amount of signal at the moment of measurement. Then:

Short TE \rightarrow effect of T_2 will be lower
 Long TE \rightarrow effect of T_2 will be more evident

TR (repetition time) is the time between two consecutive excitation pulses. If TR is left excessively long, all tissues will have time to recover equilibrium state, regardless of their respective T_1 . As a result, we will not account for differences in the tissue based on T_1 times. On the contrary, if TR is kept short, there will be substantial differences in the recovery of each tissue during that time. Then:

Short TR \rightarrow great T_1 effect
 Long TR \rightarrow low T_1 effect


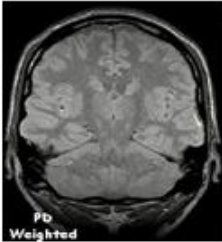

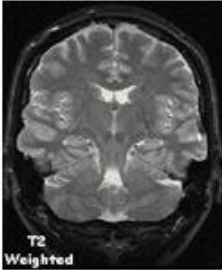
TE/TR values	SHORT TR	LONG TR
	T1 WEIGHTED IMAGE:	PROTON DENSITY IMAGE:
SHORT TE		
LONG TE		T2 WEIGHTED IMAGE: 

Fig. 1.10 TR and TE effect in MRI contrast[41]

There are three main types of pulse sequences:

1) **Spin-echo (SE)** sequences:

SE sequences are generated by two successive RF-pulses, typically a 90° - 180° (excitation-refocusing) pair. Can be single echo (90-180-90-180...) or multiple echo (90-180-180-180...; 90-180-180-180...). Single echo type produces echoes of higher amplitude, providing a higher image quality. Multiple echo type provides lower image quality but a faster acquisition

2) **Inversion recovery (IR)** sequences:

IR sequences are generated by applying an inverting 180° pulse before a normal spin echo sequence. The inversion time (TI) is the time between the initial inverting pulse and the excitation pulse. The initial inversion is used to create a T_1 contrast which can be further increased by modifying TR and TE values of the SE sequences posterior to the inverting pulses. If the excitation pulse is applied when the magnetization vector of a tissue is parallel to the transversal plane, the tissue will not be affected by the pulse and will not produce any signal contribution. Therefore, IR can also be used for tissue suppression. Despite these advantages, the IR sequences have some disadvantages like lower SNR and increased acquisition times.

3) **Gradient echo (GRE)** sequences:

GRE sequences use a magnetic field gradient to induce the formation of an echo after the excitation pulse, instead of the 180° pulses characteristic of spin echo sequences. After the excitation pulse, a first negative gradient is applied to accelerate the dephasing and therefore the decay of the FID signal. Then a second positive gradient with the same strength is applied to rephase the spins and generate the echo. Maximum amplitude decay between consecutive echoes follows a T_2^* decay instead of a T_2 decay. Therefore, the signal will be weaker but the acquisition will be much faster.

Another pulse sequence of interest is **echo planar imaging (EPI)** sequence [10]. EPI is a fast imaging sequence that consists in applying the initial 90° - 180° pulses like in SE sequence but, after the 180° pulse, the frequency encoding gradient is rapidly changed from positive to negative amplitude to generate multiple gradient echoes. This highly reduces the acquisition time, at expense of a lower spatial resolution. This fast acquisition is required when imaging rapidly changing physiological processes such as for cerebral perfusion assessment in fMRI.

Advantages and disadvantages of MRI

- ✓ MRI modality provides high resolution anatomical volumetric images, with excellent soft tissue contrast. In addition, 2D slices can be taken in any desired orientation by applying a suitable combination of gradients.
- ✓ MRI can also be used to obtain functional images of different physiological processes, like neural activation by capturing changes in the local blood flow.
- ✓ MRI includes a large variety of acquisition techniques, which allow generating different MRI contrasts for studying many anatomical regions or physiological processes.
- ✓ MRI does not involve the use of ionizing radiation like other image modalities such as X-ray/computed tomography, PET or SPECT, thus avoiding the side effects of using this kind of radiation for imaging living organisms. This is especially important for vulnerable people like pregnant women and children. Ionizing radiation has harmful effects on living organisms such as radiation-induced cancer, genetic damage or infertility.
- ✗ MRI scanning is a significantly long (~ 30 - 60 min vs. < 5 min for CT) procedure, making it prone to motion artifacts arising from movement of the patient during the scanning.

- X The narrow scanning region of the typical MRI scans, in addition to the loud noises produced during the scan and the long scanning time, can be troublesome for the patient, especially if the patient suffers from claustrophobia.
- X X-ray/CT are usually better for bone imaging, providing higher detail than MRI.
- X Patients wearing a pacemaker or a metallic implant could be rejected for undergoing an MRI scan due to possible injuries derived from malfunction of the device or movement or heating of the implant.
- X MRI scanner is more expensive than the scanners for other medical image modalities. A mid-market MRI scanner costs around 500.000 US\$ while a mid-market CT scanner costs around 120.000 US\$. A mid-market PET/CT hybrid scanner costs around 300.000 US\$. [11]. The MRI scanning procedure cost, although it depends on the MRI type, is on average more expensive too, with the exception of PET mainly due to radiotracer generation.

1.4 Cerebral perfusion imaging

One major interest for biomedical researchers in the field of neurology is the assessment of the neural activity either in resting conditions or in active conditions, that is, to study which areas of the brain become activated and the intensity of this activation when performing certain tasks.

Nowadays, there is no way to assess this activity directly, that is, to measure exact ATP production and consumption at specific areas of the brain, but there are indeed methods that allow measuring some physiological processes that can be related to ATP consumption (energy consumption).

One of these physiological processes is cerebral blood flow (CBF). Cerebral blood flow implies a glucose and oxygen delivery, which is paramount for ATP production and thus, energy gathering for increased neural activity. An increase in neural activity in a brain region translates into an increase of blood flow coming to that region, and this relationship is used to study brain activity through CBF measurement.

Currently, the main imaging modalities for studying CBF are positron emission tomography (PET) and functional MRI (BOLD fMRI and ASL).

PET

CBF assessment through PET image modality involves the injection of a radiotracer like ^{15}O labeled water [12]. The radiotracer, which travels along with the blood, experiences a radioactive decay that can be detected and located by the PET device. A higher recruitment of blood in some cerebral region implies an increased presence of radiotracer and radioactivity coming from that region. As a result, the detected signal intensity will be larger.

BOLD fMRI

BOLD (Blood-oxygen-level dependent) fMRI like PET, uses a contrast agent for obtaining the functional image but the difference resides in the contrast agent being endogenous (from the own body) and not exogenous. Therefore, BOLD fMRI is a non-invasive method for CBF assessment. The contrast agent used in BOLD fMRI is a constituent of the blood, the deoxyhemoglobin (dHb). Hemoglobin is a protein present in the red blood cells that serves as the blood oxygen carrier. Depending on oxygen saturation of hemoglobin, we can distinguish two forms of hemoglobin: oxyhemoglobin -when oxygen is bonded to Hb-, and deoxyhemoglobin -Hb without bonded oxygen-[13]. These two molecules differ in their magnetic properties: oxyhemoglobin is diamagnetic and deoxyhemoglobin is paramagnetic. When a diamagnetic substance is inside a magnetic field, it creates an internal induced magnetic field that opposes the external field. On the contrary, a paramagnetic substance creates an internal induced magnetic field in the direction of the external field [14]. Due to its paramagnetic nature, an increased concentration of

deoxyhemoglobin reduces the T2* relaxation time of the surrounding blood water protons by increasing the local dephasing of the magnetic moments. Oxyhemoglobin, does not produce this effect. Cerebral regions of higher activity require more oxygen, which is compensated by an increase in blood flow and oxyhemoglobin concentration and, in last term, a stronger signal received. The difference in signal intensity (1-5%) can be detected by T2* weighted images.

ASL

ASL is an fMRI technique that uses an endogenous contrast agent, arterial blood water for perfusion assessment. However, ASL does not exploit the spontaneous magnetic behavior of its contrast agent like BOLD fMRI but actively labels the arterial water in order to use it as a tracer. [15]

- **Acquisition principles**

The magnetic labeling consists in an inversion of the arterial blood water magnetization via an RF pulse. This labeling, which makes the labeled water to have a paramagnetic behavior, is applied prior to signal acquisition. A short time is left between the labeling and the signal acquisition to give time to the labeled arterial blood water to flow into brain tissue. The inverted spins of the labeled water will reduce the magnetization of the region, with the acquired signal joining the contributions of both labeled water and static tissue water.

Following this acquisition, a control image is taken without applying any specific labeling, so spins of arterial blood water and static tissue water have the same magnetic state.

The difference between the tag and control images gives a quantitative measurement of the arterial blood perfusion, that is, the amount of arterial blood delivered to the brain tissue. The ASL signal is expressed as the ratio:

$$ASL_{signal} = \frac{M_c - M_l}{M_c} \quad (10)$$

M_c: control image

M_l: label image

The final CBF image is obtained by applying some physiological and MR parameters (relaxation and transit times, blood-tissue water partition coefficient) to the ASL image.

- **ASL sequences**

While the labeling of arterial water before acquiring the tag image is a common procedure for all ASL modalities, there are two main types of ASL sequences depending on how this labeling is done: continuous (CASL) and pulsed (PASL). The fundamental differences between these two sequences reside in the size of the labeled region and duration of the labeling pulses.

1) CASL

CASL is characterized by a long-time continuous inversion pulse (1-3seconds) over a single thin planar region, generally located at carotid level. Arterial blood water is continuously labeled as it traverses the labeling plane. This process, known as “flow driven adiabatic inversion”, requires the labeling process to be shorter than the relaxation times and the labeling pulse to be long enough to achieve a steady state. This last condition is one of the major disadvantages of CASL. Long labeling RF pulses saturate the cerebral tissue producing a signal loss in the tag image, due to the so-called magnetization transfer effects. This leads to subtraction errors when calculating the ASL image. Practical implementation of long continuous RF pulses is usually not straightforward. Most commercial scanners do not include CASL sequences in their software because the long continuous RF pulses apply a heavy workload to the hardware components and a large RF energy deposition to the patient. Special safety measures must be taken to avoid exceeding the specific absorption rate (SAR) limits legally established for MRI [16].

To overcome the limitations of pure CASL sequence, an alternative sequence known as pseudo-continuous ASL (pCASL) is used. In pCASL, a long train of shaped RF pulses (1000 or more) are fired in very fast succession. The disadvantage of pCASL with respect to CASL is that the SNR is about 30 to 50% lower. Still, it avoids the distortion of the ASL signal and the excessive load to the hardware.

There are other CASL implementations that try to solve the limitations apart from pCASL like dual-coil ASL (DC-ASL), that requires using two separate coils for labeling and imaging, and almost continuous ASL (ACASL), in which the continuous pulse is rapidly interrupted from time to time to reduce workload on the hardware. Nevertheless, the requirement of additional hardware (DC-ASL) or magnetization transfer effects correction (ACASL) made the pCASL to arise as the main standard for CASL imaging.

2) PASL

PASL is characterized by short-time inversion pulses (typically 10-15 milliseconds) over a whole block of tissue, which is referred to as the inversion slab.

There are many PASL sequences and, although they operate on a similar basis, they present some differences in the way the inflowing spins are labeled. Three of the most popular PASL methods are: FAIR (flow-sensitive alternating inversion recovery), EPISTAR (echo planar imaging and signal targeting with alternating radiofrequency) and PULSAR (Pulsed star labeling of arterial regions)

In FAIR, the tag image acquisition step consists in an inversion of a narrow slab of tissue which contains the imaged slice. The slab is slightly wider for applying the inversion uniformly. After the inversion pulse, a delay is introduced so non-inverted spins from arterial water have time to reach the slice to be imaged and replace some of the inverted spins there by the moment the image is acquired. At control image acquisition step, an inverting pulse is applied to a selected slab of tissue but into a large area (“non-slice-selective inversion”). During control inversion, all spins have been inverted whether they are in the image slice or at carotid level. A time delay is again introduced between the non-selective inversion pulse and image acquisition, so during this time, spins from the arterial water flow into the slice to be imaged. At the time the image is acquired, the magnetizations arising from both remaining stationary inverted spins belonging to the slice and the inflow spins are approximately the same. By subtracting the control and tag image, the stationary spins contribution in the slice is removed, and a flow sensitive image is obtained. Although there are many variations of the original FAIR sequence, the most commonly used is still this original sequence.

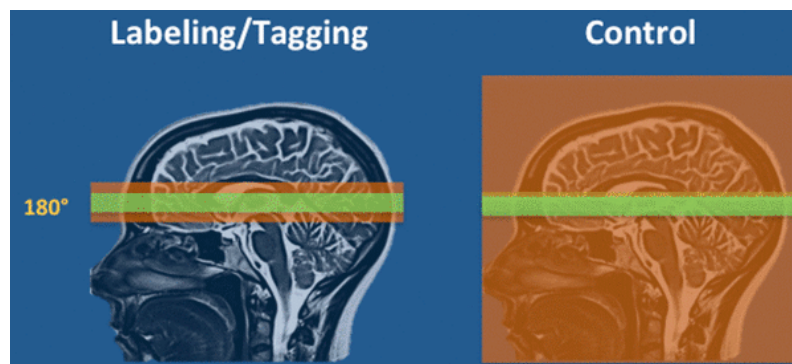


Fig. 1.11 inversion areas (red) in FAIR-MRI during slice (green) acquisition[42]

In EPISTAR, the tag image acquisition step consists in an inversion of a thick slab of tissue extending from the carotid level to a small additional region above the slice to be imaged. The control image acquisition step consists in an inversion of a symmetrical slab of tissue to the tag step but now above the slice to be imaged, plus a small additional region below it. By doing this, both image slices from the tag and control steps will have equivalent magnetization transfer effects. Like in FAIR, a time delay is introduced between the inversion pulses and image acquisitions for allowing the arterial water spins to reach the slice. Again, by subtracting the control and tag image, the stationary spins contributions in the slice are canceled out together with the magnetization transfer effects, and a suitable perfusion sensitive image is obtained.

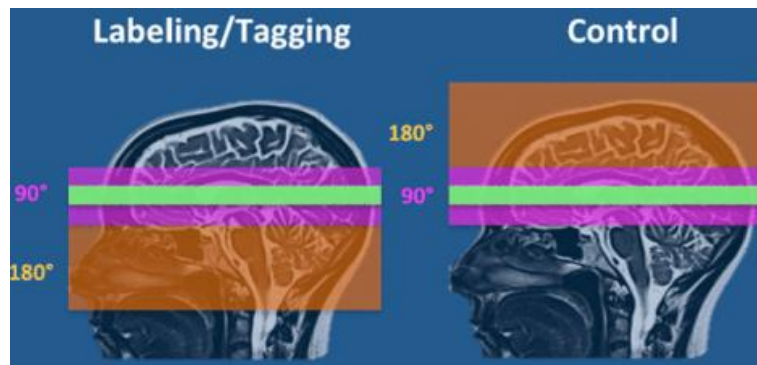


Fig. 1.12 EPISTAR slice acquisition[42]

PULSAR is a variant of EPISTAR sequence in which a water suppression pulse is included prior to the labeling step. The water suppression pulse pre-saturates the stationary spins of the water belonging to the imaging region, thus obtaining an image with increased flow sensitivity. Although PULSAR is more difficult to implement than the plain EPISTAR sequence, it has the advantages of having a larger SNR and tagging efficiency as well as being less affected by field inhomogeneities [17].

- **Comparison between CASL and PASL**

Whether to use CASL or PASL depends both on the application and the application conditions.

On one hand, CASL provides a higher SNR than PASL, especially for whole brain imaging but at the expense of a more difficult implementation of the sequence, a heavier workload on the hardware and increased magnetization transfer effects.

On the other hand, PASL, which currently stands as the choice of preference for performing ASL imaging, is easier to implement and is less affected by magnetization transfer effects, but provides a lower SNR.

Currently, pCASL is becoming the preferred option as it includes the main advantages of both CASL and PASL.

Comparison between imaging methods

PET has three main disadvantages with respect the MRI methods: it is invasive (injection of the tracer), implies working with ionizing radiation and the spatial resolution achieved is poorer.

BOLD fMRI is easier to implement than ASL and achieves a higher SNR and temporal resolution, making it a better option than ASL for studying brain activity in response to certain short events.

ASL, in turn, achieves better spatial resolution than BOLD and provides a quantitative measurement (BOLD is only qualitative/ relative percent changes). Furthermore, BOLD shows a strong low frequency noise component, making it inadequate for long event

response experiments. This low frequency noise is not present in ASL, which is frequency independent as the time interval between tag and control images is very short [18].

1.4 The partial volume effect problem in ASL imaging

For obtaining a suitable CBF volumetric image that reflects brain activity at a given time, the time interval between consecutive ASL signal acquisitions, (acquisition of consecutive tag/control image pairs) must be as short as possible. For that reason, fast imaging techniques such as EPI are employed, accomplishing the required fast acquisition times at the expense of spatial resolution.

The MRI image is composed by a 3D array of cubic elements known as voxels, which are analogous to the pixels in the 2D images. The spatial resolution of the MRI image is determined by the voxel size, which defines the smallest detail we are able to distinguish in the image. A small voxel size allows differentiation of small details, thus translating into a good spatial resolution, whereas large voxels translate into a poor spatial resolution.

As a result of the fast imaging methods, ASL (and BOLD) images have poor spatial resolutions (voxel size $\sim 2 \times 2 \times 4 \text{mm}$) with respect to a typical anatomical MRI images ($\sim 0.5 \times 0.5 \times 1 \text{mm}$). Spatial resolution is usually around 4 times lower for ASL than for anatomical MRI.

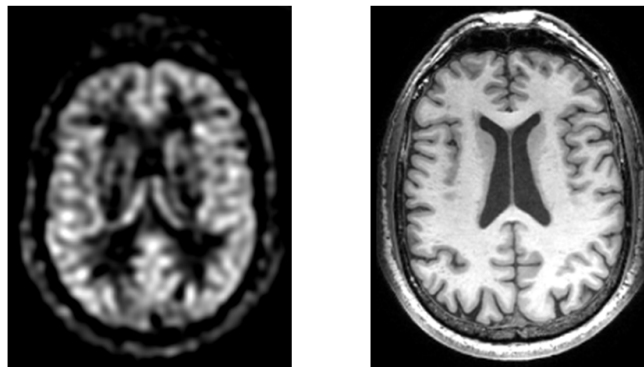


Fig. 1.13 ASL and anatomical MRI resolution comparison

Three different tissue collections can be distinguished along the brain:

1) Gray matter (GM), which consists mainly of neuronal cell bodies and is located at the cerebral surface composing the cerebral cortex

2) White matter (WM), which consists mainly in myelinated axons and is located beneath the cortex

3) Cerebrospinal fluid (CSF), which provides mechanical protection as well as chemical regulation of the brain.

Because of the limited spatial resolution, many voxels in the ASL image are heterogeneous, meaning that the cubic element does not contain a single tissue type but more than one of those tissues inside it. This fact, which is referred to as partial volume effect (PVE), causes a signal cross-contamination as the measured ASL signal in each of those voxels results from the summation of all individual contributions of the tissues contained in the voxel.

$$\frac{\Delta M}{M_c} = \frac{P_{GM} \cdot \Delta M_{GM} + P_{WM} \cdot \Delta M_{WM} + P_{CSF} \cdot \Delta M_{CSF}}{P_{GM} \cdot M_{GM} + P_{WM} \cdot M_{WM} + P_{CSF} \cdot M_{CSF}} \quad (11)$$

ΔM : difference between control and label images ($M_c - M_l$)

ΔM_i : signal contribution of tissue i

P_i : partial tissue fraction of tissue i

The motivation of applying methods for correcting the PVE is to determine the individual contributions of GM and WM and CSF to the ASL image. As mentioned in the beginning of this document, some studies relative to neurodegenerative diseases such as Alzheimer and dementia [1] suggest the prior emergence of hypoperfusion in specific cerebral regions before developing the characteristic tissue atrophies of the advanced stages of the disease. An early diagnosis of these diseases is very important firstly, in terms of treatment planning and patient's life quality and secondly, for carry on scientific research that would allow a deeper understanding on the degenerative process.

In the majority of the cases, the research interest is focused over the GM perfusion. Thin cortical regions and regions close to the interface between two tissue types are specially affected by PVE due to the large pixel sizes. Due to this fact, it is fundamental to rely on effective partial volume correction (PVC) methods to discriminate the individual perfusion of GM from that of WM and CSF (which is normally assumed to be zero).

1.5 State of the art

Currently, the most used methods for PVC of ASL images are the PET legacy algorithm and the Asllani's regression algorithm.

PET legacy algorithm

A common method for PVC of PET CBF images that has been extended to ASL images is based on the overall observed brain GM/WM perfusion ratio [19]. The approach often consists in two steps:

The first step consists in estimating the fractional tissue volumes for GM, WM and CSF corresponding to each voxel in the ASL image. These values (P_{gm} , P_{wm} and P_{csf}) are estimated by the segmentation of a high resolution anatomical MRI from the same subject. The segmentation procedure gives three tissue probability maps each of which containing the respective tissue fractions for each voxel. The summation of the fractional tissue volumes is always equal to 1. Then, the probability maps masks are preprocessed so that tissue fractions lower than a given threshold value (commonly 20%) are discarded from the corresponding tissue mask. This is usually done over the GM mask, as it is the tissue of interest in most of the studies. The GM mask is then overlaid to the ASL image to obtain a GM perfusion image.

The second step consists in the correction of the GM perfusion voxels having $P_{gm} < P_{wm} + P_{csf}$. Commonly, CSF fluid contributions are assumed to be zero. GM perfusion value for those voxels are corrected by assuming that GM perfusion is equal to WM perfusion multiplied by a fixed chosen factor (typically 2.5). The final corrected value for a voxel located at position (i, j, k) is calculated as:

$$V_{corr}(i, j, k) = \frac{V_{obs}(i, j, k)}{\frac{1}{f} + P_{wm}(i, j, k)} \quad (12)$$

V_{corr} : GM corrected perfusion value

V_{obs} : perfusion value observed in the ASL image

f : GM/WM mean perfusion factor

P_{wm} : WM tissue fraction

Although this approach is simple and straightforward, it leads to errors in the individual perfusion due to underestimation or overestimation of this value. The mean perfusion values for each type of tissue are not equal and so are not the mean signal intensities that are obtained from each of them. Signal intensity for GM is on average, higher than the corresponding to WM and this later is in turn higher than that for CSF. As a result, voxels having $P_{gm} > P_{wm} + P_{csf}$ would be classified as GM only, no correction would be applied and the GM perfusion values would be underestimated.

Conversely, the correction applied to voxels having $P_{gm} < P_{wm} + P_{csf}$, although taking into account the mean perfusion differences between GM and WM, may not be very accurate, as the same fixed factor is arbitrarily imposed over all these voxels.

To avoid these estimation errors, it is necessary to use other alternative and more complex methods that attempt discriminating the individual perfusion values more accurately.

Asllani regression algorithm

Asllani algorithm [20] models the voxel intensity as a summation of all individual contributions of the tissues contained in the voxel. The signal contribution of each type of tissue in a voxel will be thus described by the following equations:

$$M = M_{GM} + M_{WM} + M_{CSF} \quad (13)$$

$$M_{GM} = P_{GM} \cdot m_{GM} \quad (14)$$

$$M_{WM} = P_{WM} \cdot m_{WM} \quad (15)$$

$$M_{CSF} = P_{CSF} \cdot m_{CSF} \quad (16)$$

M: net voxel intensity in the original CBF image

M_j: intensity contribution of tissue j

P_j: tissue fraction of tissue j

m_j: CBF corresponding to tissue j

If we develop the net voxel intensity equation (13):

$$M = P_{GM} \cdot m_{GM} + P_{WM} \cdot m_{WM} + P_{CSF} \cdot m_{CSF} \quad (17)$$

The tissue fractions are obtained, like for the previous method, from a high resolution MRI by co-registering it to the ASL image and then segmenting the co-registered image to get the corresponding GM, WM and CSF tissue probability maps.

The next figure shows a diagram of this process together with the central slices in axial direction of images that result from each step:

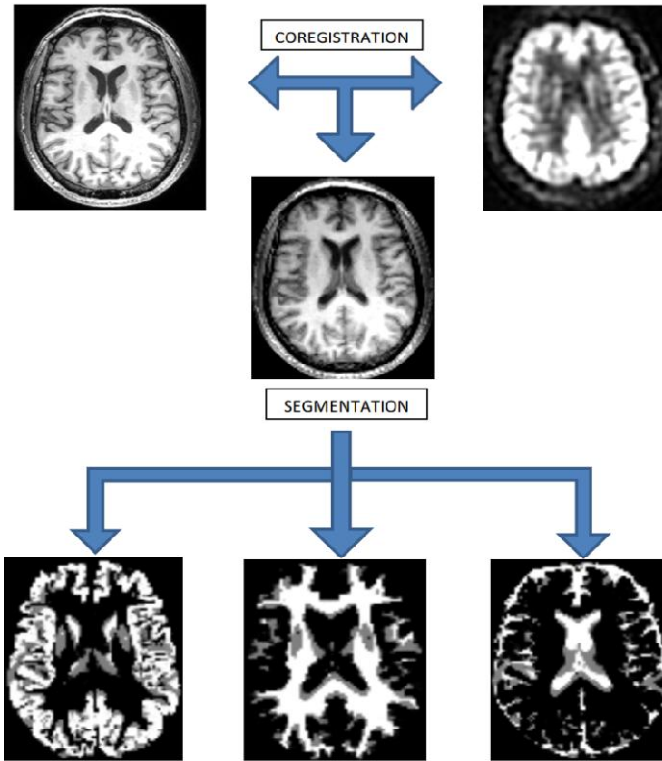


Fig. 1.14 spatial preprocessing step before PVC (coregistration & segmentation)

For each voxel in the image there is one equation and three unknowns: m_{gm} , m_{wm} and m_{csf} . Therefore, it is not possible to solve the unknowns by using only the information given by a single voxel intensity. By taking the assumption that the perfusion values m_{gm} , m_{wm} and m_{csf} are equal for the neighbor voxels ($m_{gm}(i) = m_{gm}$; $m_{wm}(i) = m_{wm}$; $m_{csf}(i) = m_{csf}$) a system of equations can be build and solved by linear regression :

$$\begin{cases} M(i) = P_{GM}(i) \cdot m_{GM} + P_{WM}(i) \cdot m_{WM} + P_{CSF}(i) \cdot m_{CSF} \\ \dots \end{cases} \quad (18)$$

where i denotes the neighbor pixel i to the central pixel to be solved

Considering a regression kernel of size $n \times n$ centered at a voxel j , we can express the above system of equations in matrix form:

$$[P]\vec{x} = [M] \quad (19)$$

$[P]$: $n^2 \times 3$ matrix containing the tissue fractions for GM, WM and CSF in each column

\vec{x} : 3×1 column vector with the unknown local CBF values for GM, WM and CSF respectively

$[M]$: $n^2 \times 1$ column vector containing the observed intensity values of the voxels

\vec{x} can be solved by linear least square regression, being the solution:

$$\vec{x} = ([P]^t * [P])^{-1} * [P]^t * [M] \quad (20)$$

Therefore, for each voxel of the image, a system of linear equations is defined from the original CBF values of this voxel and the neighboring voxels, together with their

respective tissue probabilities. By solving the respective system, we can obtain the estimated GM, WM and CSF perfusion values for the central voxel. In other words, three new CBF maps for GM, WM and CSF are estimated from the original CBF image and the segmented image volumes after the correction process. CSF perfusion is usually assumed to be zero and discarded.

The Asllani's algorithm includes an additional condition, which will be referred as the Asllani condition. The Asllani condition states that a voxel will be considered for the regression analysis if at least 3 voxels over the neighborhood contain some $P_i > 0$ for all i ; i.e. if at least three voxels have some amount of all tissue types; otherwise the perfusion values for that voxel are set to zero. This condition has a double purpose: first, it excludes the voxels belonging to background from the analysis and second, it ensures that $[P]^t * [P]$ is non-singular and the pseudo-inverse $([P]^t * [P])^{-1}$ can be calculated.

The assumption of perfusion uniformity over the neighborhood around the central voxel causes the regression kernel to introduce blurring over the output CBF maps. In the work done by Asllani et al., the regression algorithm performance was evaluated by calculating the root mean-square error (RMSE) for different kernel sizes: 3x3x1, 5x5x1, 7x7x1, 9x9x1, 11x11x1 and 15x15x1. RMSE was calculated separately for GM and WM perfusion by computing the error over voxels having $P_{gm} > 0.8$ and $P_{wm} > 0.8$ respectively. They obtained the following average RMSE errors after applying the PVC over seven subjects:

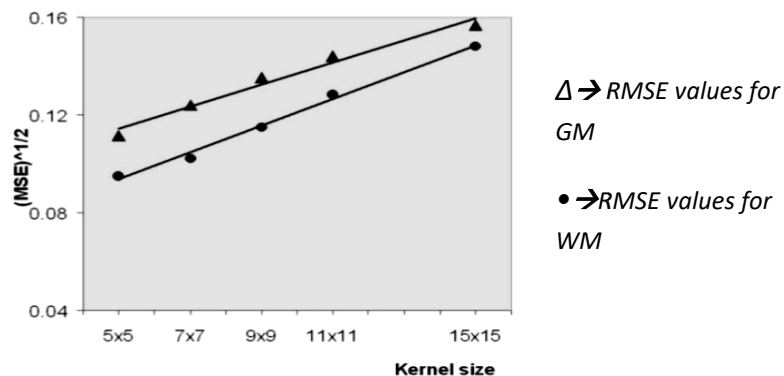


Fig. 1.15 RMSE value vs regression kernel size[20]

The conducted evaluation proved that the larger the kernel size, the higher the RMSE error in both GM and WM cases because of the increased blurring effect and worse holding of the local perfusion uniformity assumption. The results for 3x3x1 were not reported in the study because the Asllani condition failed at many voxels due to the reduced kernel size, leading to an erroneous output in which many voxels belonging to brain tissue were set directly to zero.

CHAPTER 2: 3DWLS algorithm for PVC

The 3D weighted least squares (3DWLS) algorithm for PVC of ASL images was presented in the International Society for Magnetic Resonance in Medicine (ISMRM) congress of 2015 [21]. The **contribution of this bachelor thesis** was:

- 1) Implement this algorithm as a program (Python)
- 2) Propose two new weighting methods (inverse exponential, Gaussian) for the least squares regression
- 3) Evaluate the correction performance depending on the parameters chosen (kernel size and weighting type applied)
- 4) Compare the results with the Asllani's correction algorithm

2.1 Algorithm description

The 3DWLS algorithm is based on the algorithm developed by Asllani et Al. The 3DWLS shares the voxel intensity model of the Asllani's algorithm, in which such intensity value corresponds to the summation of the GM, WM and CSF partial contributions. Those contributions are estimated, equally, by a least square linear regression from the voxel intensities of the original image and the partial tissue fractions of each voxel. Likewise, the tissue fractions are obtained through co-registering and posterior segmentation of a high resolution anatomical image.

The 3DWLS introduces two improvements with respect the Asllani's algorithm:

- **Use of a 3D kernel instead of a 2D kernel**

Asllani's algorithm uses a 2D kernel, that is, if we consider the volumetric CBF image as a stack of image slices, it uses the information provided by the neighbors of the central voxel along the same slice for solving the regression problem. Therefore, it does not take into account the information contained in the neighboring voxels of superior and inferior slices.

The 3DWLS, in turn, uses a 3D kernel using the information of the closest voxels to the central voxel in all directions of the space, and not only in the slice plane. In advance, this supposes an advantage over the 2D kernel for two reasons:

-Firstly, depending on the voxel size and the kernel size, it is possible that the closest neighborhood around the central voxel is the one including the voxels belonging to superior and inferior slices instead of in-plane voxels that are more distant to the central voxel. To illustrate this, we can take as an example an ASL image having a typical voxel size of $2 \times 2 \times 4$ mm along \vec{x} , \vec{y} and \vec{z} axis respectively, being $\vec{x}\vec{y}$ the direction that defines the slice planes and \vec{z} the direction perpendicular to those planes. If we select a kernel size of $5 \times 5 \times 1$, the most distant voxels of the kernel (those

corresponding to the corners of the square kernel) would be located at $\sqrt{4^2 + 4^2} \approx 5.56 \text{ mm}$ from the center of the kernel. On the other hand, if we select a 3D kernel of size 3x3x3, the most distant voxels of the kernel (those corresponding to the corners of the cuboid kernel) would be situated at 4.9 mm.

The following figures illustrate the distance matrixes for two kernels with size 5x5x1 and 3x3x3 for correcting a hypothetical ASL image with a voxel size of 2x2x4 mm. Each element corresponds to a voxel, being the one highlighted in blue the central voxel of the kernel. The values of each element represent the Euclidean distance of this element to the central voxel in mm.

5.66	4.47	4.00	4.47	5.66
4.47	2.83	2.00	2.83	4.47
4.00	2.00	0.00	2.00	4.00
4.47	2.83	2.00	2.83	4.47
5.66	4.47	4.00	4.47	5.66

Fig. 2.2 5x5x1 distance matrix [D]

4.90	4.47	4.90
4.47	4.00	4.47
4.90	4.47	4.90

2.83	2.00	2.83
2.00	0.00	2.00
2.83	2.00	2.83

4.90	4.47	4.90
4.47	4.00	4.47
4.90	4.47	4.90

Fig. 2.1 3x3x3 distance matrix [D]

Thus, in terms of satisfying the assumption of perfusion uniformity over the proximities of the central voxel, the 3x3x3 kernel would be better than the 5x5x1 kernel.

-Secondly, by using a 3D kernel, blood flow changes along \vec{z} result more continuous and anatomically consistent as regression is not solved simply slice by slice, but including the information of the superior and inferior slices.

- **Weighting of the neighbor voxels influence depending on their distance to the central voxel**

Perfusion uniformity is assumed along the immediate proximities to the central voxel. As we get further from the center of the kernel towards its boundaries, the steadiness of this assumption is weaker. Due to this fact, the 3DWLS introduces a weighting as a function of the voxel distance to the center of the kernel so that data of closer voxels are given more importance than the distant voxels in the regression analysis.

Three different distance-weighting kernels ($[W_d]$) as a function of the distance have been explored in this work: inverse of the distance, inverse exponential of the distance and Gaussian of the distance. Prior to the weighting type selection, a distance matrix

[D] of the same size that the regression kernel is calculated (see fig. 15 & 16). Voxel dimensions are generally different for each spatial axis: x and y dimensions (in the slice plane) are usually equal and smaller than z dimension (the direction perpendicular to the slices). Because of this, [D] must be constructed from the real voxel size (in mm) and not simply from the distance in voxels from the center. If the latter is done, taking the previous voxel size example (2x2x4mm), adjacent voxels to the central voxel along \vec{x} and \vec{y} would receive the same weighting than the adjacent pixels along the \vec{z} but in fact, the last are further away from the center according to the actual voxel size of the image.

The distance matrix [D] is constructed by setting central element to zero and each one of the remaining elements to the value of the real Euclidean distance between that element and the central element depending on the image voxel size. This step is common to all three weighting matrix types. Depending of the weighting type [W_d] is calculated from [D] as follows:

1) Inverse of the distance

The central element is set to 1 and then, the values of the remaining elements are inverted, that is:

$$W_{dist}(i, j, k) = \frac{1}{D(i, j, k)} \quad (21)$$

ijk denotes element position being $(i,j,k)=(0,0,0)$ the central position

The following figure illustrates the shape and values of W_{dist} for a kernel size of 5x5x3 voxels:

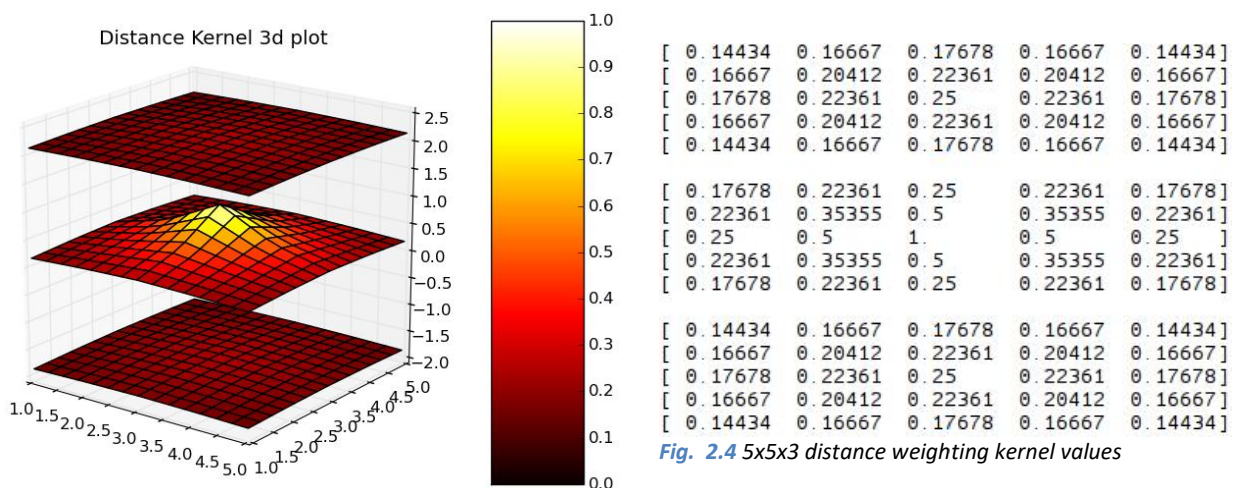


Fig. 2.4 5x5x3 distance weighting kernel values

Fig. 2.3 3D plot of 5x5x3 distance weighting kernel(interpolated)

2) Inverse exponential of the distance

$$W_{exp}(i, j, k) = e^{-D(i,j,k)} \quad (22)$$

The following figure illustrates the shape and values of W_{exp} for a kernel size of 5x5x3 voxels:

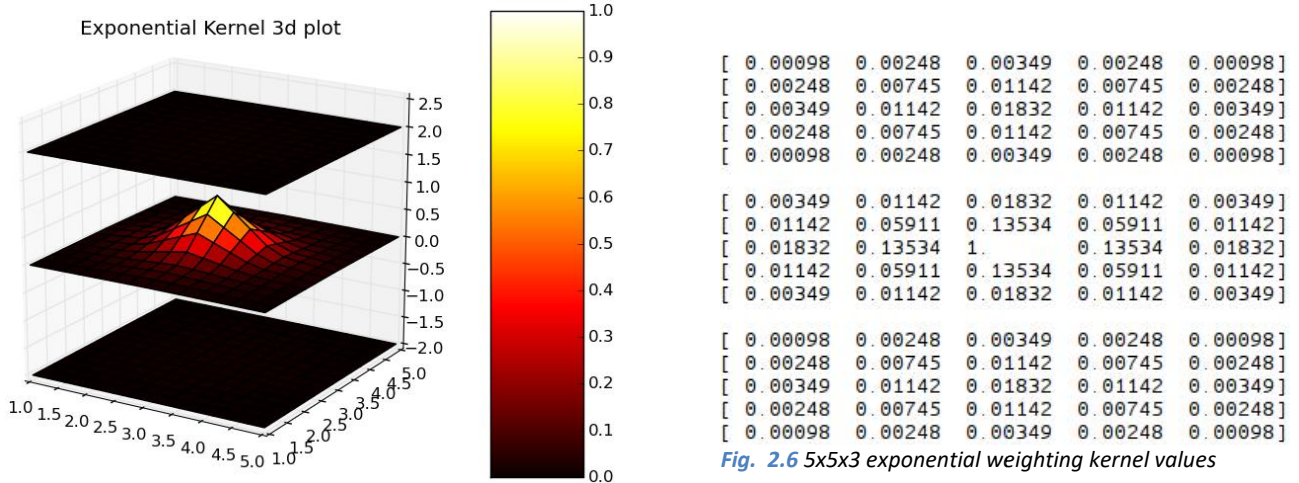


Fig. 2.5 3D plot of 5x5x3 exponential weighting kernel(interp.)

Fig. 2.6 5x5x3 exponential weighting kernel values

3) Gaussian of the distance

The weighting kernel in this case will be the Gaussian of the distance values according to the Gaussian equation:

$$W_{gauss}(i, j, k) = A \cdot e^{\frac{-[D(i,j,k)-\mu]^2}{2\sigma^2}} \quad (23)$$

The mean value μ is set to zero for the Gaussian maximum to be centered at zero distance i.e. to start the decay at the central position of the kernel.

Coefficient A determines the value of the maximum of the Gaussian function; being the value attained at the center equal to A, which was chosen to be equal to 1.

With the mean and A coefficient values chosen the above expression reduces to:

$$W_{gauss}(i, j, k) = e^{\frac{-D(i,j,k)^2}{2\sigma^2}} \quad (24)$$

σ coefficient determines the width of the Gaussian function, i.e. the steepness of its decay from the central initial value $A=1$. It was decided for W_{gauss} to have a weighting value of 0.67 at the closest distance (min_{dist}) from the center of the kernel.

This value is the result of choosing a proper σ depending on the closest distance (which is dependent in turn, to the voxel size). The suitable sigma value results from the following equation:

$$\sigma = \frac{\min_{\text{dist}}}{\sqrt{-2 \ln(V)}} \quad (25)$$

V: desired closest weighting value (in our case, 0.67)

As dimensions are consistent over the whole CBF image, the weighting kernel only needs to be calculated once and it is moved and centered over each voxel of the image like the regression kernel, during the iteration over the image elements.

The following figure illustrates the shape and values of W_{gauss} for a kernel size of 5x5x3 voxels:

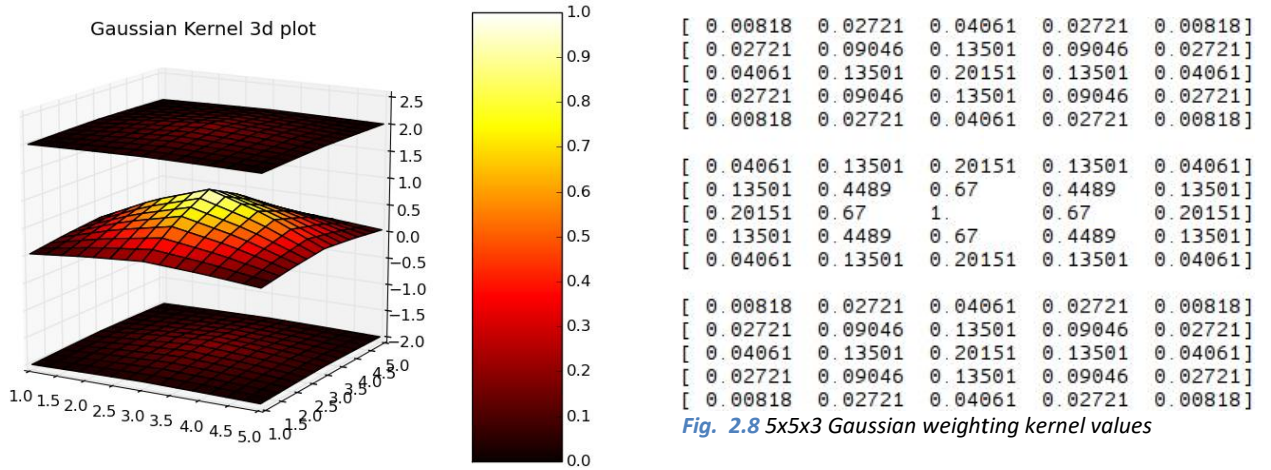


Fig. 2.8 5x5x3 Gaussian weighting kernel values

Fig. 2.7 3D plot of 5x5x3 Gaussian weighting kernel(interp.)

In addition to the weighting matrix as a function of the distance, another weighting matrix as a function of tissue heterogeneity of the voxels was explored. This matrix, which was called fractional aniso-probability matrix ($[W_{FA}]$) is calculated from the tissue probability maps resulting after segmentation of the co-registered anatomical image. As previously explained, each voxel of the ASL image is assigned three tissue probabilities from these maps (P_{gm} , P_{wm} and P_{csf}) whose summation is always equal to 1. For example, a voxel having $P_{gm} = 0.5$, $P_{wm} = 0.5$ and $P_{csf} = 0$ would be composed by gray and white matter in equal proportion, with no cerebrospinal fluid present. The FA weighting coefficients are calculated from the tissue probabilities using the following equation:

$$W_{FA}(x, y, z) = \frac{1}{\sqrt{2 \cdot [P_{gm}(x, y, z) + P_{wm}(x, y, z) + P_{csf}(x, y, z)]^2}} \sqrt{[P_{gm}(x, y, z) - P_{wm}(x, y, z)]^2 + [P_{wm}(x, y, z) - P_{csf}(x, y, z)]^2 + [P_{csf}(x, y, z) - P_{gm}(x, y, z)]^2} \quad (26)$$

xyz denotes voxel position in the ASL image

Voxels having a higher degree of heterogeneity are penalized while voxels composed mainly of one tissue type have a higher weighting coefficient.

$[W_{FA}]$ matrix is calculated in one go before starting the iteration over the voxels of the ASL image, yielding a matrix of the same size as the image. At each iteration step, the elements of $[W_{FA}]$ overlapping with the regression kernel ($[W_{FA}(k)]$) are used for the weighting.

Both $[W_D]$ and $[W_{FA}(k)]$ can be combined by multiplying both matrixes elementwise, yielding a final weighting matrix $[W]$ whose elements are calculated by:

$$W(i, j, k) = W_D(i, j, k) \cdot W_{FA}(k)(i, j, k) \quad (27)$$

Recalling the system of linear equations resulting from the application of the regression kernel, the least-square solution to the system $[P]\vec{x} = [M]$ in the presence of a weighting matrix $[W(k)]$ is:

$$\vec{x} = ([P]^t * [W(k)]^{-1} * [P])^{-1} * [P]^t * [W(k)]^{-1} * [M] \quad (28)$$

Before starting the iteration process, the CBF image is preprocessed by multiplying this image to the brain mask obtained from the summation of the three tissue probability maps. Voxels belonging to brain tissue have a value of 1 in this mask while voxels not belonging to brain tissue have a value of zero. By multiplying the original CBF image and the mask elementwise, the intensity values of the voxels belonging to brain tissue are kept, while all non-zero background intensity values (due to noise) are set to zero.

During the iteration process, if a kernel centered at a given voxel does not contain any voxel with intensity higher than zero, the computation moves onto the next voxel. Thus, by this preprocessing, all background voxels are easily excluded from the analysis and the computation is faster.

Regarding the Asllani condition, a modified version of this condition was introduced. The new condition also states that the kernel must include at least three voxels with some amount of tissue, but not necessarily all three types of tissue like Asllani condition. By introducing this change, we avoid discarding valid voxels belonging to brain regions that have only one or two types of tissue. This wrong discarding of valid pixels, as previously said, is notorious in the case of small regression kernels (3x3x1, 5x5x1) because in some brain regions there are not three voxels present having all three types of tissue around the reduced neighborhood of the central voxel.

However, by being less restrictive with the condition, singularity problems are re-introduced. In neighborhoods lacking one or two tissues, the columns corresponding to those tissues in the matrix $[P]$ have all their elements equal to zero, thus being $[P]$ a

rank deficient matrix. This fact causes $[P]^t * [P]$ to be singular so it does not have an inverse and the regression solution \vec{x} cannot be calculated.

Nevertheless, it is fair to say that if a region does not contain a certain tissue, the individual perfusion contribution of that tissue is null. So, by dropping the zero columns from the analysis and modeling the voxel perfusion as the sum of the individual contributions of the remaining tissues, the rank deficiency of $[P]$ is avoided, together with the singularity problems.

2.2 Algorithm evaluation

Materials

The algorithm was tested over 15 artificial perfusion maps generated from the MNI-152 anatomical template, created by the Montreal Neurological Institute and available at <http://www.bic.mni.mcgill.ca/ServicesAtlases/ICBM152NLin2009>.^(C) 1993–2004 Louis Collins, McConnell Brain Imaging Centre, Montreal Neurological Institute, McGill University). This template consists on a T1-weighted image resulting from averaging the T1 anatomical images of 152 subjects. The tissue probability maps of this template image are also provided in the MNI webpage.

The artificial perfusion maps were generated in MATLAB® (The MathWorks, Inc). Following the voxel intensity model described before, the maps were created from a sum of simulated individual contributions of GM, WM and CSF. These individual contributions were set to adequate average perfusion values for GM, WM and CSF inside the real expected range of values. Furthermore, in order to include some variability in the simulated perfusion values, a noise was introduced with a standard deviation approximately equal to the standard deviation observed among real subjects.

Both the simulated perfusion ranges and the standard deviations chosen are based in the work by Parkes et Al.[21], in which they investigate the average GM and WM perfusion as well as the standard deviation of these measurements between 34 subjects (15 males and 19 females).

The obtained GM and WM average values (in $ml_{blood} * 100 ml_{tissue}^{-1} * min^{-1}$) in this work were:

$$\begin{aligned} \text{Males} & \begin{cases} Avg_{gm} = 58 \pm 13 \\ Avg_{wm} = 23 \pm 3 \end{cases} \\ \text{Females} & \begin{cases} Avg_{gm} = 68 \pm 10 \\ Avg_{wm} = 25 \pm 5 \end{cases} \end{aligned}$$

The average perfusion values for the artificial maps were randomly chosen within those ranges. For CSF perfusion, the chosen range was [2 - 5].

The next table illustrates the chosen average perfusion values for each of the 15 artificial CBF maps created for testing the algorithm:

Map nº	Avg_{gm}	Avg_{wm}	Avg_{csf}
1	63	26	4
2	72	28	4
3	68	26	4
4	62	26	3
5	53	24	3
6	53	25	3
7	52	23	2
8	75	30	5
9	50	22	2
10	49	22	2
11	73	29	5
12	53	23	2
13	70	28	4
14	53	23	2
15	77	30	5

Three different types of artificial perfusion maps were generated in terms of the kind of noise introduced. The noise standard deviations selected were:

$$Std_{gm} = 12$$

$$Std_{wm} = 5$$

$$Std_{csf} = 1$$

- **TYPE 1: Normally distributed random noise (Maps 1-5)**

The high resolution simulated perfusion maps (CBF_{tissue}) are obtained as follow:

$$CBF_{gm}(x, y, z) = P_{gm}(x, y, z) \cdot N_{NormGM}(x, y, z) \quad (29)$$

$$CBF_{wm}(x, y, z) = P_{wm}(x, y, z) \cdot N_{NormWM}(x, y, z) \quad (30)$$

$$CBF_{csf}(x, y, z) = P_{csf}(x, y, z) \cdot N_{NormCSF}(x, y, z) \quad (31)$$

N_{norm} : matrix of equal size as P , whose values follow a normal distribution centered at AVG_{tissue} and with a standard deviation of Std_{tissue}

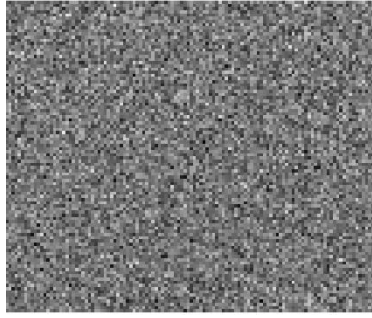


Fig. 2.9 normal random noise for simulated CBF maps

After the generation of the above simulated maps, their spatial resolution is reduced to match that of a typical ASL imaging resolution, approximately 2x2x4 mm. This was done by downsampling the above maps using trilinear interpolation.

The following figures show the central slices in axial direction of one set of downsampled artificial perfusion maps (type 1):



Fig. 2.10 Artf. GM perfusion (Type 1)

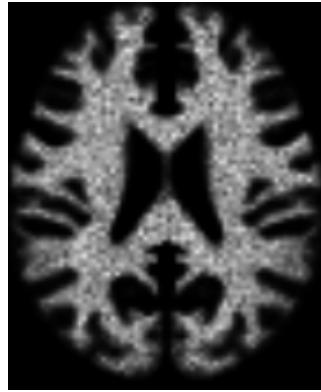


Fig. 2.11 Artf. WM perfusion (Type 1)

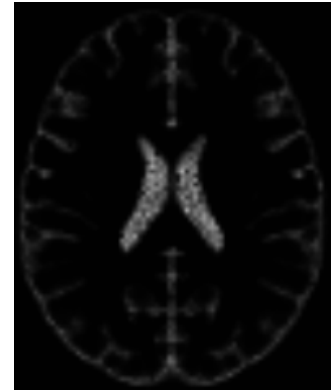


Fig. 2.12 Artf. CSF perfusion (Type 1)

The final simulated perfusion map results from adding up all these partial contributions:

$$ASL_{sim} = CBF'_{gm} + CBF'_{wm} + CBF'_{csf} \quad (32)$$

CBF' : downsampled version of CBF

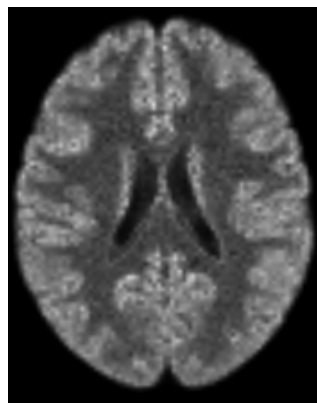


Fig. 2.13 Artf. ASL image (Type 1)

- **TYPE 2: sinusoidal & random noise (Maps 6-10)**

The sinusoidal noise results from the summation of two 2D sinusoidal signals of equal amplitude and offset, which oscillate along perpendicular directions: sagittal and coronal. Regarding the number of oscillations along the image dimensions, 10 oscillations along sagittal direction and 15 oscillations along coronal direction were chosen, leading to the following noise images:



Fig. 2.14 sinusoidal noise for type 2 artificial CBF map generation

The amplitude and offset of the sinusoidal noise is defined by the standard deviation and average perfusion value of each tissue. For the case of the sinusoidal signal for GM perfusion of a map i , the amplitude value would be equal to $\frac{Std_{GM}(i)}{2}$ and its offset would be equal to $Avg_{GM}(i)$. The amplitude and offset values for the WM and CSF sinusoidals are defined analogously from their own standard deviation and average values.

Furthermore, a random noise has been added to the sinusoidal signals. This additional noise takes random values inside the range 85%-100% of the average perfusion value of each tissue in each map.

The high resolution simulated perfusion maps (CBF_{tissue}) are obtained as follow:

$$CBF_{gm}(x, y, z) = P_{gm}(x, y, z) \cdot N_{SinGM}(x, y, z) + N_{RandGM}(x, y, z) \quad (33)$$

$$CBF_{wm}(x, y, z) = P_{wm}(x, y, z) \cdot N_{SinWM}(x, y, z) + N_{RandWM}(x, y, z) \quad (34)$$

$$CBF_{csf}(x, y, z) = P_{csf}(x, y, z) \cdot N_{SinCSF}(x, y, z) + N_{RandCSF}(x, y, z) \quad (35)$$

N_{sin} : matrix of equal size as P , containing the described cross-sinusoidal signals in each slice

N_{rand} : matrix of equal size as P , which contains the random noise described above

As in the previous case, these maps are downsampled by trilinear interpolation to match the ASL spatial resolution.

The following figures show the central slices in axial direction of one set of downsampled artificial perfusion maps (type 2):



Fig. 2.15 Artf. GM perfusion (Type 2)

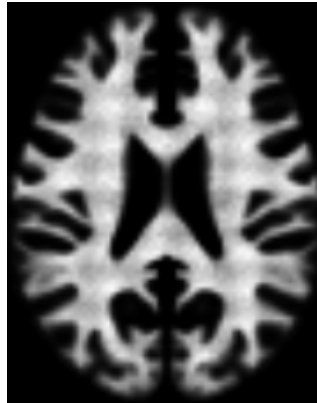


Fig. 2.16 Artf. WM perfusion (Type 2)



Fig. 2.17 Artf. CSF perfusion (Type 2)

The final simulated perfusion map results, like in the previous case, from the addition of all these partial contributions.

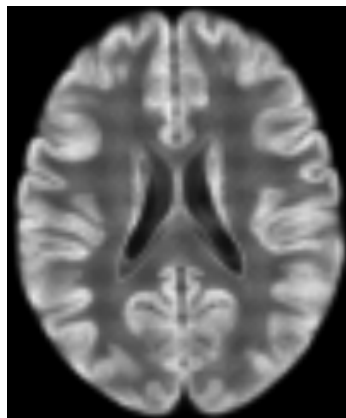


Fig. 2.18 Artf. ASL image (Type 2)

- **TYPE 3: simulated atrophies (maps 11-15)**

The last type of artificial perfusion maps is generated as the type 1 maps, but including 5 different simulated perfusion atrophies (hypoperfusion and/or hyperperfusion regions). The hypoperfusion and hyperperfusion atrophies consist in including a decrease (to 30%) and an increase (to 170%) in the perfusion values respectively, along a spherical region in the simulated image. The chosen radius for the spherical regions was 15 mm. The atrophy masks generated are filtered by a Gaussian blurring filter before applying them to the perfusion maps. This application is done by elementwise multiplication of the mask and the perfusion map.

The following figures show the simulated ASL images with atrophies that were generated (maps 11-15)

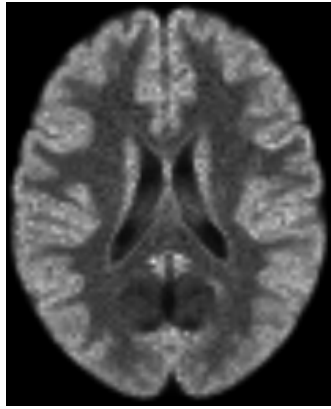


Fig. 2.19 Atrophy 1. two overlapping hypoperfusion regions in GM

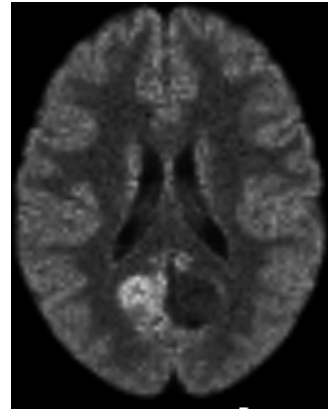


Fig. 2.20 Atrophy 2. two overlapping hypoperfusion and hyperperfusion regions in GM

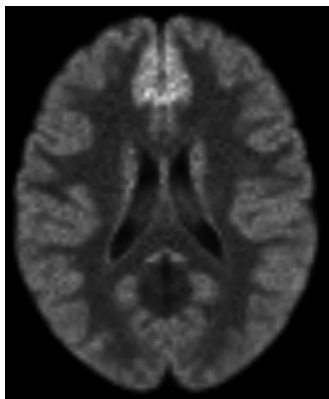


Fig. 2.21 Atrophy 3. two non-overlapping hypoperfusion and hyperperfusion regions in GM

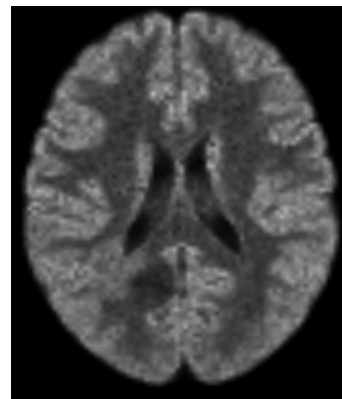


Fig. 2.22 Atrophy 4: GM hypoperfusion atrophy overlapping a WM hyperperfusion atrophy

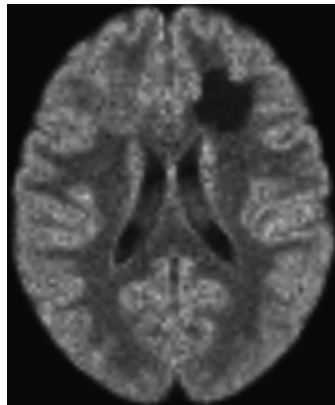


Fig. 2.23 Atrophy 5: two non-overlapping hypoperfusion and hyperperfusion regions in WM

Methods

The algorithm was tested by performing a PVC of the final simulated perfusion maps using the 3DWLS algorithm with different regression kernel sizes and weighting types. PVC was also done using an implementation of Asllani's algorithm with different regression kernel sizes to compare both algorithms. For the algorithms to operate under the same conditions, the Asllani condition was substituted by the modified condition in the implementation.

The evaluation was carried out by comparing the root mean square error (RMSE) between the original partial perfusion maps used to generate the final simulated perfusion maps and the partial maps obtained from the PVC of the latter.

$$RMSE_t = \frac{1}{n_t} \sum \sqrt{[CBF'_t - Out_t]^2} \quad (36)$$

t : denotes tissue (GM, WM or CSF) or total image (sum of partial perfusions)
 \sum : denotes summation of all matrix elements
 n_t : total number of t voxels $\rightarrow \sum([P_t])$
 Out_t : corrected perfusion image for tissue t

Four different analyses were run over each of the 15 simulated images. The regression kernel sizes chosen for the case of 3DWLS were: 3x3x3, 5x5x3, 5x5x5, 7x7x3, 7x7x5 y 9x9x5; and for the Asllani's case: 3x3x1; 5x5x1, 7x7x1, 9x9x1, 11x11x1.

The resulting RMSE values were averaged over the image group to yield a single RMSE value for each parameter combination in each analysis.

Results

PVC by 3DWLS with $W = W_D \cdot W_{FA}(k)$

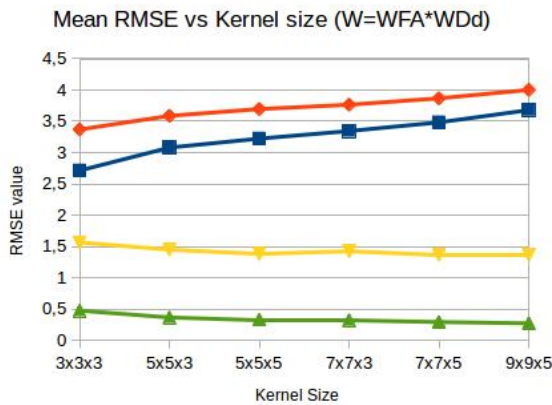


Fig. 2.24 RMSE values using distance weighting and FA

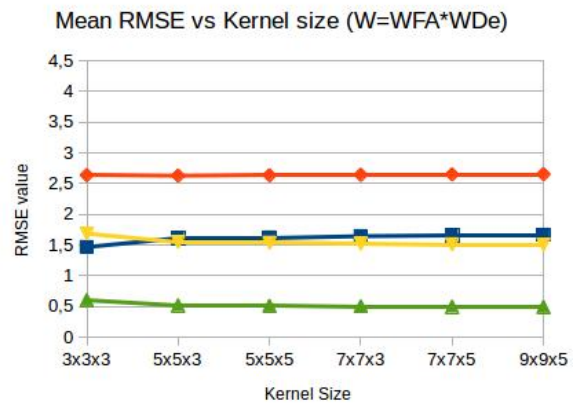


Fig. 2.25 RMSE values using exponential weighting and FA

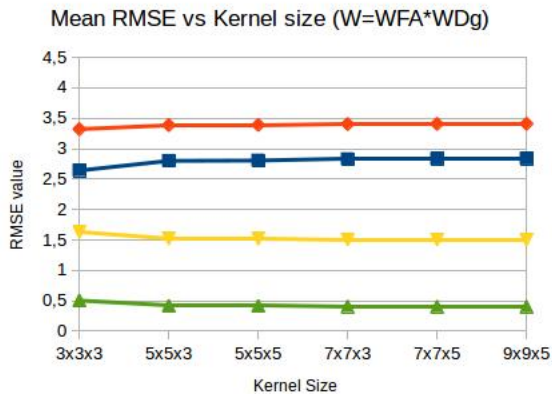


Fig. 2.26 RMSE values using Gaussian weighting and FA



PVC by 3DWLS with $W = W_D$

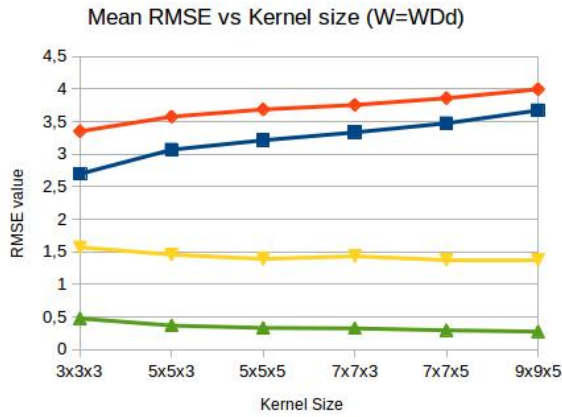


Fig. 2.27 RMSE values using distance weighting

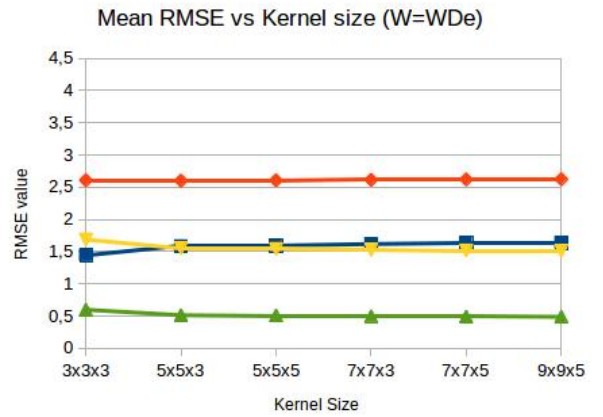


Fig. 2.28 RMSE values using exponential weighting

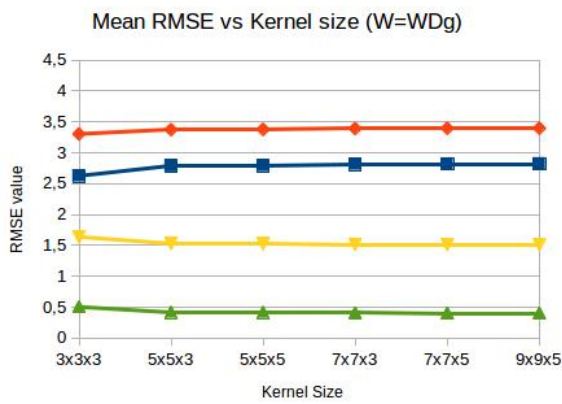


Fig. 2.29 RMSE values using Gaussian weighting



PVC by 3DWLS with $W = W_{FA}$

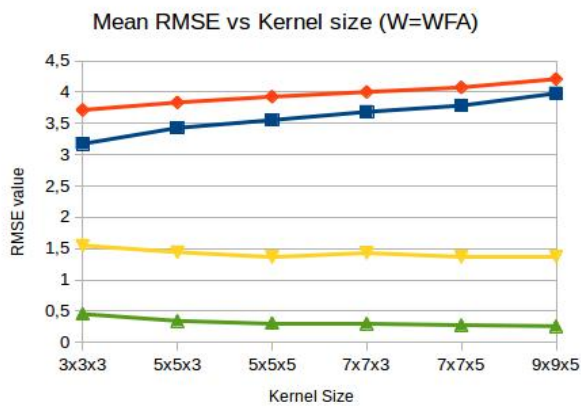


Fig. 2.30 RMSE values using FA

PVC by Asllani's algorithm

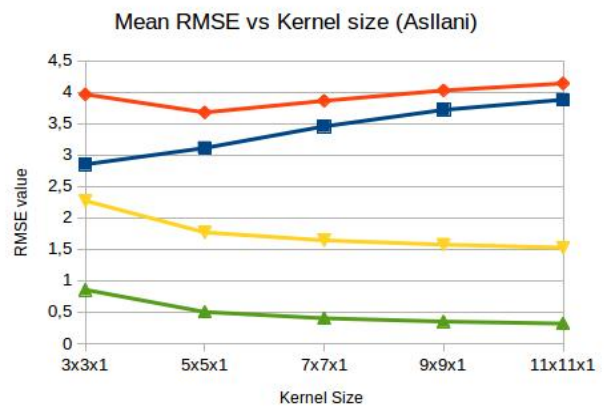


Fig. 2.31 RMSE values using Asllani's algorithm

To test the performance of the algorithm over the atrophy regions, an additional evaluation was carried out, calculating the RMSE values over those regions alone.

The resulting RMSE values were averaged like before, yielding the following results:

PVC on atrophy regions by 3DWLS with $W = W_D \cdot W_{FA}(k)$

Average Atrophy RMSE vs Kernel size (W=WFA*WDd)

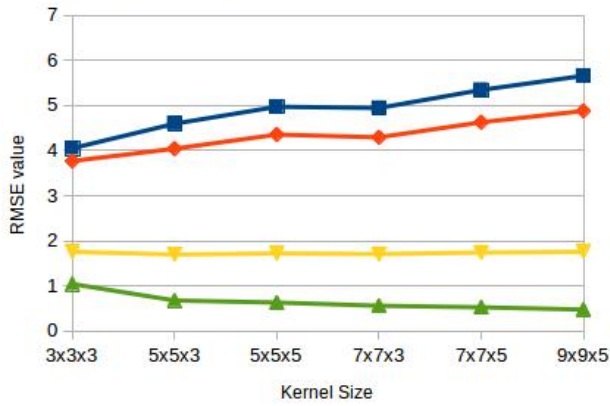


Fig. 2.32 RMSE values on atrophies using distance weighting and FA

Average Atrophy RMSE vs Kernel size (W=WFA*WDe)

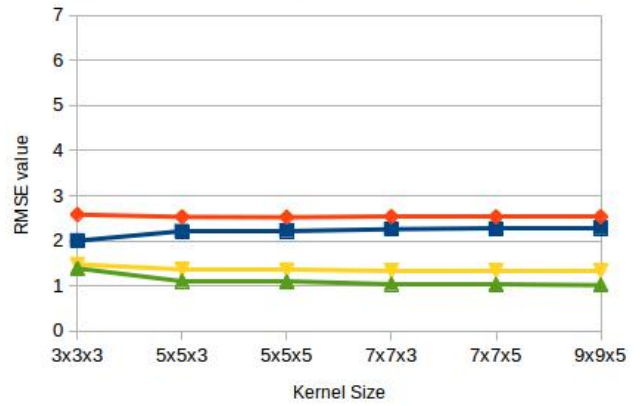


Fig. 2.33 RMSE values on atrophies using exponential weighting and FA

Average Atrophy RMSE vs Kernel size (W=WFA*WDg)

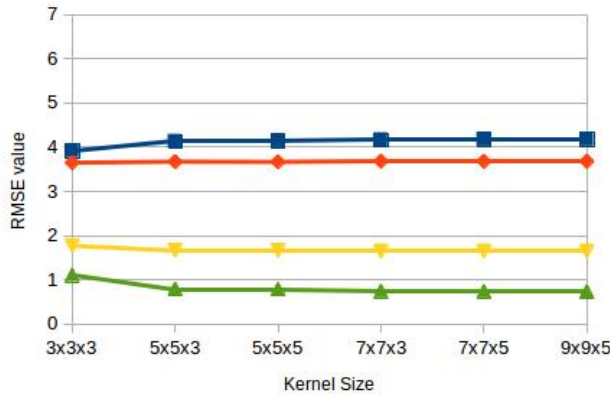


Fig. 2.34 RMSE values on atrophies using Gaussian weighting and FA



PVC of atrophy regions by 3DWLS with $W=WD$

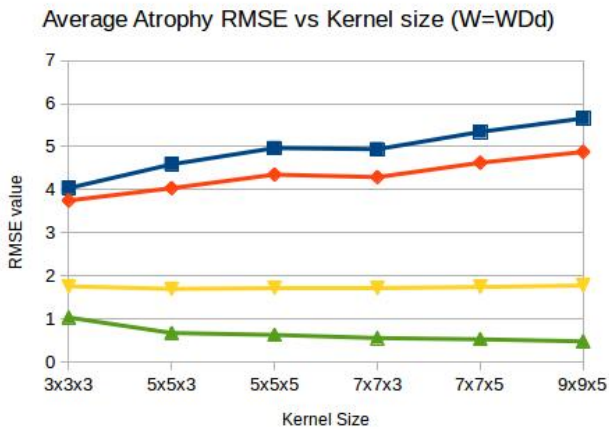


Fig. 2.35 RMSE values on atrophies using distance weighting

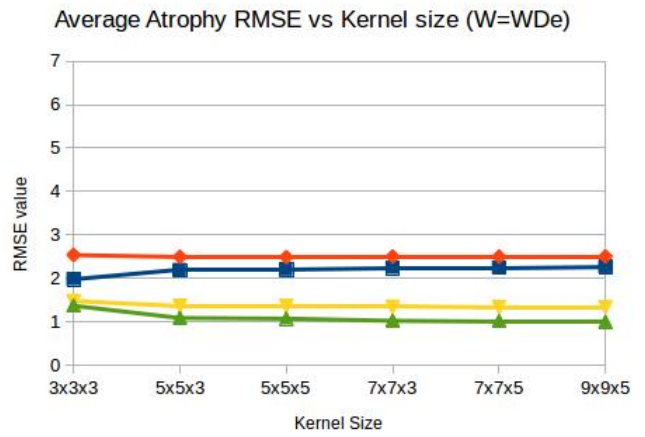


Fig. 2.36 RMSE values on atrophies using exponential weighting

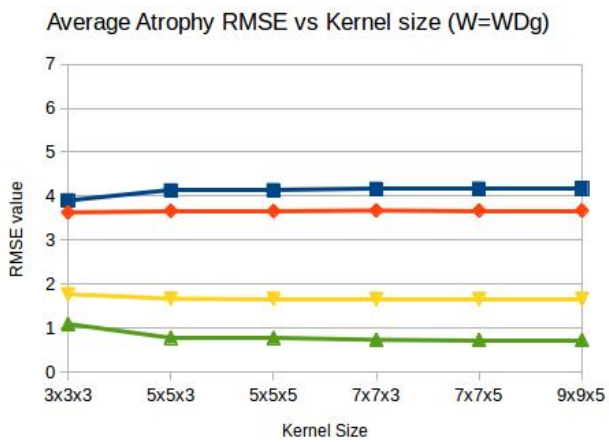


Fig. 2.37 RMSE values on atrophies using Gaussian weighting



PVC of atrophy regions by 3DWLS with $W=WFA$

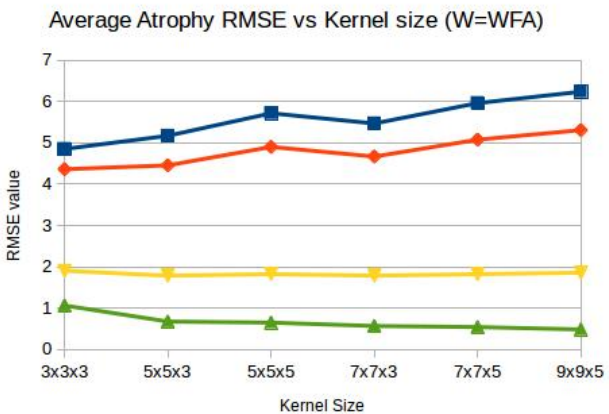


Fig. 2.38 RMSE values on atrophies using FA

PVC of atrophy regions by Asllani's algorithm

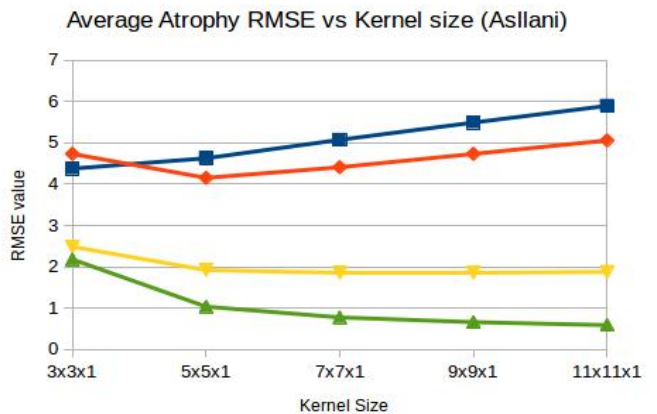


Fig. 2.39 RMSE values on atrophies using Asllani's algorithm

In all the conducted evaluations, it is appreciable that increasing the kernel size does not have a significant effect for the cases of the Gaussian and inverse exponential weighting. This happens due to the exponential behavior of both kernels (see equations 22 & 24), which makes the distant voxels of the weighting kernel to rapidly take almost negligible values. The low coefficients resulting for the voxels present in the upper and lower slices of this weighting kernels make them to approximate to 2D kernels. Because of this, an additional evaluation (with maps 1-10) was carried out to asses if using a small 3D kernel size (3x3x3) supposed any advantage to just applying the weighting kernels in a 2D way (3x3x1):

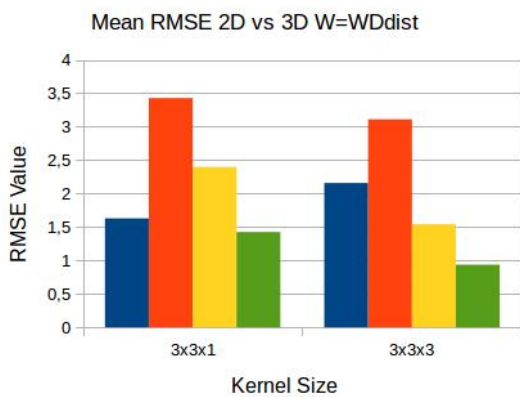


Fig. 2.40 RMSE values 2D vs. 3D using distance weighting

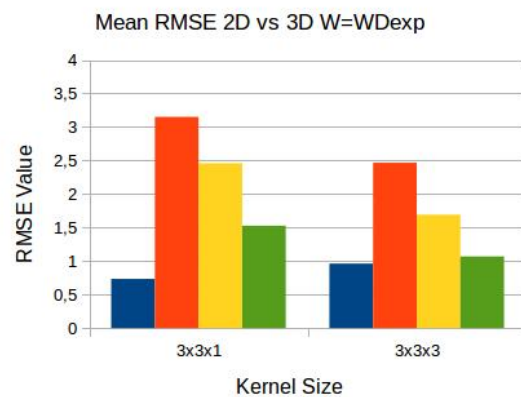


Fig. 2.41 RMSE values 2D vs. 3D using exponential weighting

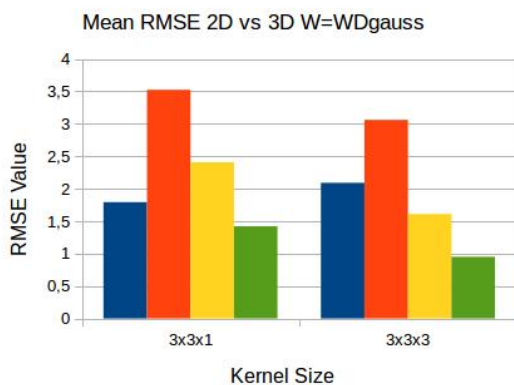


Fig. 2.42 RMSE values 2D vs. 3D using Gaussian weighting

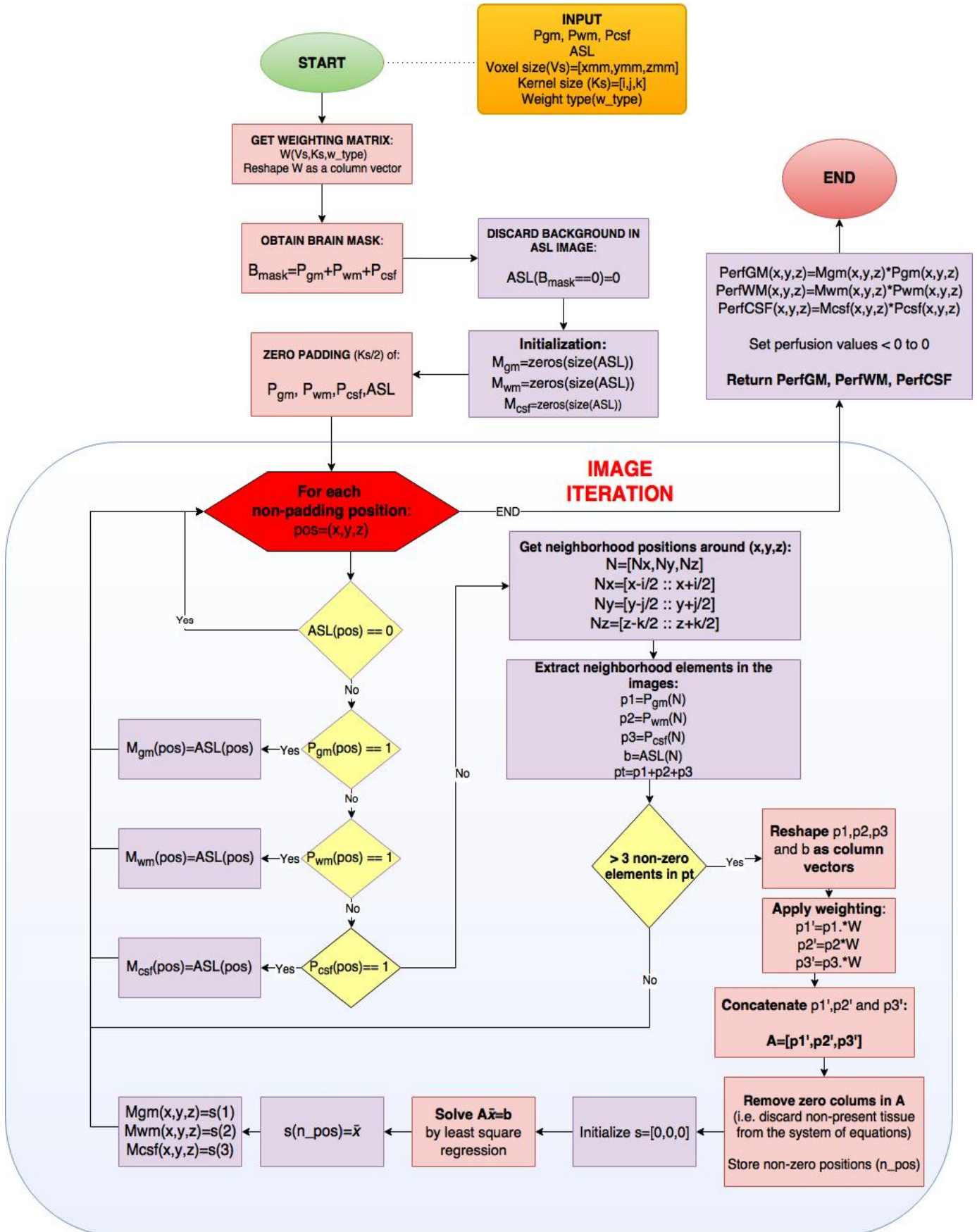


Discussion

According to the presented results, we can extract the following conclusions:

- The larger the regression kernel size, the higher the blurring effect introduced and the higher the RMSE for the general CBF image and for the GM individual perfusion. This happens both in the evaluation using the complete images and in the evaluation over the atrophy regions. For WM and CSF, a higher kernel size reduces the error. However, the increment of the error for GM resulting from a larger kernel size is more accused than the decrement of the error for WM or CSF. Thus, the best option is to choose the smallest kernel size as possible.
- Among the used weighting matrices, the inverse exponential distance weighting matrix gives substantially better results for the general and GM cases, thus being the preferred option.
- The fractional aniso-probability weighting matrix is not effective for reducing the error of the PVC. Regardless of being used in combination with the distance weighting matrices or alone, the error values obtained are equal or higher than when using distance weighting alone.
- A 2D application of the 3DWLS kernels gives a slightly lower RMSE error for the total image comparison than a 3D application. However, the latter gives quite better results for GM, WM and CSF for all weighting types. Thus, it is concluded that 3D application supposes an advantage over 2D application.
- The selection of a 3D kernel in combination with a weighting matrix represents an improvement with respect the 2D kernel used by Asllani. Regardless of the type of distance weighting, better error values are obtained with respect Asllani's algorithm. When applying the inverse exponential of the distance weighting, the total RMSE error is $\approx 52.2\%$ lower; the GM RMSE error is $\approx 29.7\%$ lower and the WM RMSE is $\approx 5.5\%$ lower.

2.3 3DWLS flowchart



CHAPTER 3: 3D Slicer extension

As a complementary work to the development and evaluation of the 3DWLS, a GUI extension that implements the algorithm has been created for 3DSlicer [22]. The extension communicates with another software package, the statistical parametric mapping (SPM) (FIL, Wellcome Trust Centre for Neuroimaging, UCL <http://www.fil.ion.ucl.ac.uk/spm/>), to carry out the functionalities required -but not exclusive- to the image correction process i.e. coregistration, segmentation and normalization.

Both 3DSlicer and SPM software suites will be briefly described in the following section. All extension functionalities are described in the 'extension features' section.

3.1 Extension dependencies

- **3DSlicer**

3DSlicer is an open source software platform for the analysis, processing and visualization of medical images widely used in the research field. The 3DSlicer framework facilitates developers the integration of new features and algorithms to the platform in an easy way, as well as creating user interfaces that implements those features for their practical use.

This framework provides native features for importing and exporting data and medical images in multiple formats and for image visualization in 2D and 3D. As a whole, the included features allow visualizing the results obtained from the implemented algorithms, evaluating their performance and introduce any required modifications easily.

The implemented extension makes use of the importation, exportation and visualization features (built on VTK and MRML libraries) as well as on the GUI widgets (built on Qt and CTK libraries) included in the 3DSlicer core. 3DSlicer provides Python wrappers for this features and the extension has been programmed in Python as a scripted loadable module.

- **SPM**

The SPM software is an open source MATLAB collection of functions for the spatial processing and statistical analysis of brain neuroimaging data (PET, fMRI).

The extension makes use of the spatial pre-processing (coregistration, segmentation and normalization) functions provided by SPM v.12. It was decided to use the SPM12 functions instead of the ones available in 3DSlicer because they are currently one of the gold standards for performing the spatial processing over brain images and are extensively used by the research community.

The extension implements an interface for communicating with the SPM MATLAB routines. This communication is based on the generation of batch script text files loadable by SPM and the execution of the batch scripts by a standalone version of SPM (available for download upon request) via a system terminal command. The SPM standalone version is a version of the SPM toolbox that has been compiled by the MATLAB compiler runtime (MCR), which is freely downloadable from the MATLAB webpage. Therefore, the extension does not require a full MATLAB installation to work.

3.2 Features description

The developed extension includes the following functionalities:

- **Importation and visualization of the ASL and anatomical images**
- Interaction with SPM software package for image **spatial processing**
- Optional **importation of an alternative image** for obtaining the **coregistration** transformation
- Optional **importation of a label image for computing PVC independently** for each of the labeled regions.
- **Regression kernel size selection** as well as **weighting type selection**
- **Normalization and smoothing** (by VTK library) of the **PVC results** for future group comparisons.
- **Exportation and visualization of the PVC results.**

The screenshot displays the GUI for the 3DSlicer extension. It features several input fields and controls:

- Path to SPM directory: [text field] [dropdown] [button ...]
- Path to matlab compiler runtime directory: [text field] [dropdown] [button ...]
- ASL image volume file: [text field] [dropdown] [button ...]
- Anatomical MRI image volume file: [text field] [dropdown] [button ...]
- Use an alternative image volume for anatomical MRI coreg + reslice:
- Alternative image volume file: [text field] [dropdown] [button ...]
- Use a label volume to perform PVC independently for each region:
- Label image volume file: [text field] [dropdown] [button ...]
- Color LUT .txt file: [text field] [dropdown] [button ...]
- Output directory: [text field] [dropdown] [button ...]
- Kernel size in pixels (x,y,z): [3] [3] [3] (spinners)
- ...in mm (x,y,z): [text field]
- Choose weighting kernel type: Exponential (dropdown)
- Normalize the output images:
- Norm. output voxel size in mm (x,y,z): [2.00] [2.00] [4.00] (spinners)
- Apply VTK gaussian smoothing to the output:
- Standard deviations in mm (x,y,z): [2.50] [2.50] [5.00] (spinners)
- Radius factors: [1.0] [1.0] [1.0] (spinners)
- Apply 3DWLS (button)

Fig. 3.1 complete view of the 3DSlicer extension GUI

Importation and visualization of ASL and anatomical images.

The minimum input required for computing the PVC is the ASL image to be corrected and a T1-weighted anatomical high resolution image of the same subject. Currently, the only supported image format is .nii format.

The images are loaded by introducing their file paths in their corresponding file path selectors. The introduction can be done both manually by typing the complete path through the keyboard or by exploring and opening the path in the file explorer window that pops up when clicking in the (...) button. Once a proper file path has been introduced, the corresponding .nii image is automatically loaded and displayed in the 3DSlicer visualization area.

ASL image volume file: ...

Anatomical MRI image volume file: ...

Fig.3.2 image importation widget and example

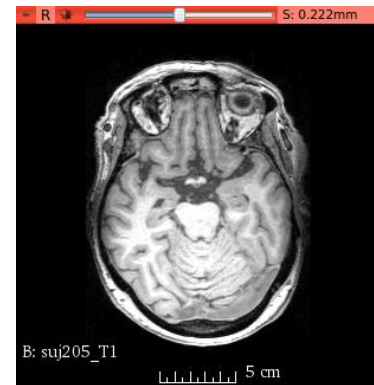


Image spatial processing

The 3DWLS algorithm requires having the tissue probability maps to estimate the partial GM, WM and CSF intensity contributions to the CBF image. These tissue probability maps are obtained through the coregistration and later segmentation of the anatomical image.

As previously said, both processing steps are conducted through SPM. During execution, the extension builds a new batch file from a template batch text file (contained in the extension folder) including the proper code lines with the paths to the current ASL and anatomical images previously imported. This final batch file is executed by sending a system terminal command that calls SPM and MCR over the file.

The user must introduce the paths to the SPM standalone and MCR directories in the system. This introduction only needs to be done once. The extension generates or modifies a text file contained in the extension folder that stores and imports these paths each time the extension is loaded in 3DSlicer.

- **Coregistration**

Image coregistration stands for the spatial alignment of two or more images belonging to the same or different subjects (intra-inter subject) and to the same or different image modality (intra and inter modality). The coregistration process consists in finding a suitable image transformation (rotation, scaling, translation...) which minimizes a cost function (sum of squared differences, correlation, mutual information...) related to the difference between the images after applying the transformation. Depending on whether the coregistration is intra or inter modality a proper cost function must be chosen. Through coregistration, the anatomical image is aligned and downsampled (to

the same size as the ASL image) to obtain a new anatomical image that overlaps to the ASL image.

- **Segmentation**

Image tissue segmentation refers to the classification and separation of the tissue captured in an anatomical image. In the case of brain images, segmentation refers to the classification of brain tissue into GM, WM, CSF and other tissues like bone. Although there are many segmentation approaches, the method implemented in SPM is based on the alignment of the anatomical image to an already classified template image for obtaining the prior probability of the voxel to contain GM, WM or CSF tissues. These prior probabilities are combined with the voxel information to obtain the tissue classification. By segmenting the coregistered anatomical image, the required tissue probability maps P_{gm} , P_{wm} and P_{csf} , are obtained.

The results from the coregistration and segmentation, that is, the coregistered anatomical volume and the three segmentation volumes for GM, WM and CSF tissues, are saved in .nii format inside the output folder specified.

Alternative coregistration

The extension allows the user importing an additional image volume (like a proton density image) for calculating the coregistration transformation to the T1 weighted anatomical image.

This coregistration transformation is later applied over the ASL image so the alternative image volume must be already in alignment to the imported ASL image and have the same matrix size.

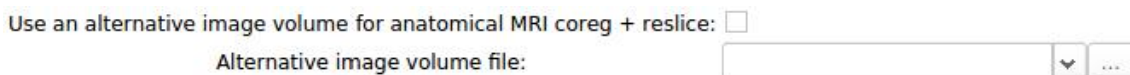


Fig. 3.3 alternative image importation widget

To apply this functionality, the option must be checked and a proper image must be introduced.

This feature is sometimes useful for improving the coregistration result, as the ASL image is very noisy and provides a poor anatomical detail.



Fig. 3.4 T1 image (sagittal slice)

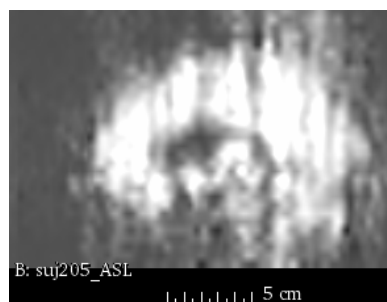


Fig. 3.5 ASL image (sagittal slice)

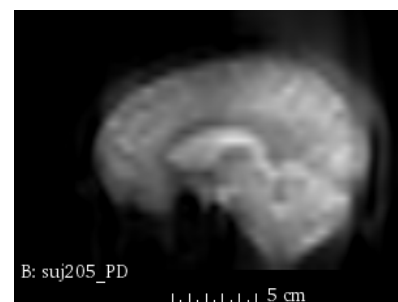


Fig. 3.6 PD image (sagittal slice)

Independent PVC per brain regions

The extension allows the user importing a label image volume containing a parcellation of specific brain regions. In a label image, voxel intensities represent region classification, i.e all voxels belonging to the same region will share the same intensity value. The regions are interpreted from the intensity values using a look-up table (LUT). As a default, the extension loads (from a text file in the extension folder) the LUT characteristic to Freesurfer, which is one of the most used software packages to estimate brain parcellation. Nevertheless any custom LUT defined by the user can be imported, provided it is given in a text file with a proper format readable by 3DSlicer.

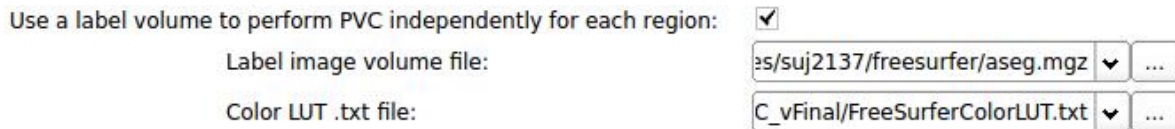


Fig. 3.7 label image and LUT importation widget

Once loaded, the label image volume is displayed in the 3DSlicer visualization area with the colors and labels defined by the selected LUT file.

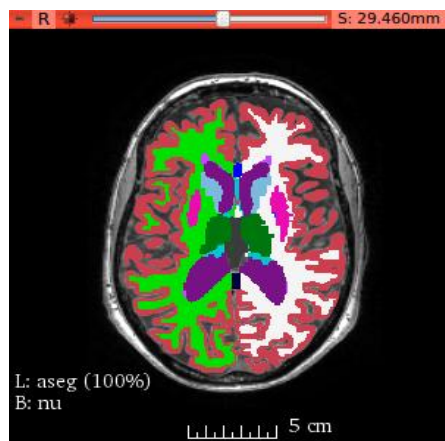


Fig. 3.8 label image displayed over a T1 anatomical image

If a label image is imported, it will also be coregistered to the ASL image so the coregistered label image will be also in alignment to the tissue probability maps. If this option is checked and a proper label image is introduced, the PVC will be done independently for each of the labeled regions.

For each region, a mask is applied to the ASL image to preserve only the voxels corresponding to that region and then the PVC is run. The final GM, WM and CSF corrected volumes result from the integration of the analogous individual maps for all the regions into single image volumes.

In addition, by applying this functionality, the extension dumps specific data(mean GM, WM and CSF perfusion and total mean perfusion)relative to each of these regions in the output data file (described later).

This feature was included taking into account an hypothesis by which the perfusion uniformity assumption will hold more likely along voxels of the same region rather than for voxels close in distance but belonging to different cerebral regions.

One drawback of this feature is that, as PVC runs over it region at a time, the computing time is longer than when applying the PVC to the whole image with a single shot.

Regression kernel size and weighting type selection

The user can select the regression kernel \vec{x} , \vec{y} and \vec{z} size (row, column and slice directions respectively) in pixels in increments of two, starting from the lowest size (3x3x1). The real size in mm of the selected kernel is displayed below the kernel size selector and it is calculated from the voxel size information contained in the ASL image .nii file.

The user can also select between the distance weighting types discussed before: inverse of the distance, inverse exponential of the distance and Gaussian of the distance.



Fig. 3.9 kernel size and weighting type selection widgets

Normalization and smoothing of PVC results

Normalization consists in anon-rigid transformation by which an image is deformed commonly to match the shape of a certain image template. Normalization is done via SPM through a batch file executed through a terminal command, like coregistration and segmentation steps. The segmentation step requires a previous normalization of the coregistered anatomical image to a template. This normalization transformation is stored and used for the normalization of the PVC output maps, the anatomical map and the original ASL image, if the user has checked the normalization option. The user can also select the voxel size of the images resulting after normalization.

Image normalization is necessary when making a group comparison. Human brains have significant differences in shape and size between different subjects. Due to this fact, the functional images of each of these subjects must be deformed to match a common image template if a physiological feature (in our case, blood flow) over a region is to be compared between the subjects.

Image smoothing can also be useful in group comparisons by reducing the effect of both structural differences and random noise, although it also reduces the image spatial resolution. Smoothing is provided in the extension by making use of the Gaussian blurring function already implemented inside the VTK library, an open source

software package for image processing and visualization. The user can select the desired parameters of the VTK Gaussian smoothing, namely, the radius factor and the standard deviation of the Gaussian filter.

Normalize the output images:	<input checked="" type="checkbox"/>
Norm. output voxel size in mm (x,y,z):	2.00 2.00 4.00
Apply VTK gaussian smoothing to the output:	<input checked="" type="checkbox"/>
Standard deviations in mm (x,y,z):	2.50 2.50 5.00
Radius factors:	1.0 1.0 1.0

Fig. 3.10 normalization and smoothing widgets

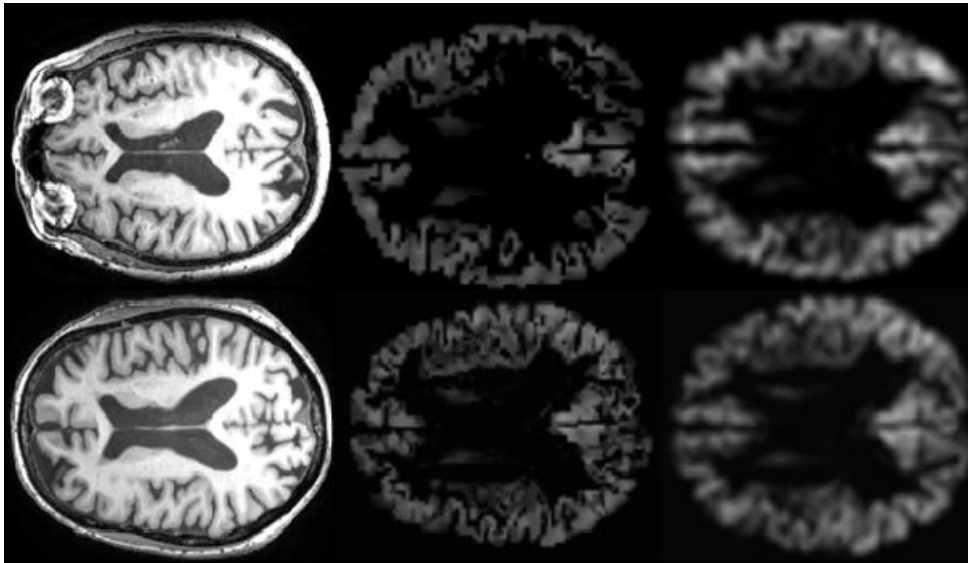


Fig. 3.11 example of normalized output. Each row is a different subject. The columns from left to right represent subject anatomical image, subject GM perfusion after correction and norm. GM perfusion

Together with the normalization template, the extension folder contains its corresponding label and tissue segmentation volumes. By selecting the normalization feature, both are coregistered to the corrected perfusion images and then stored in the output folder.

As normalization step is posterior to the correction, the template label volume does not influence the correction step, but is used for obtaining the mean perfusion values of each of the brain regions defined in the label map. These values are exported to the text data file for their comparison between different subjects.

Exportation and visualization of PVC results

By default, the extension creates the output folder inside the ASL image directory but the user can select any alternative directory.

Output directory:

 ▼ ...

Fig. 3.12 output folder selector widget

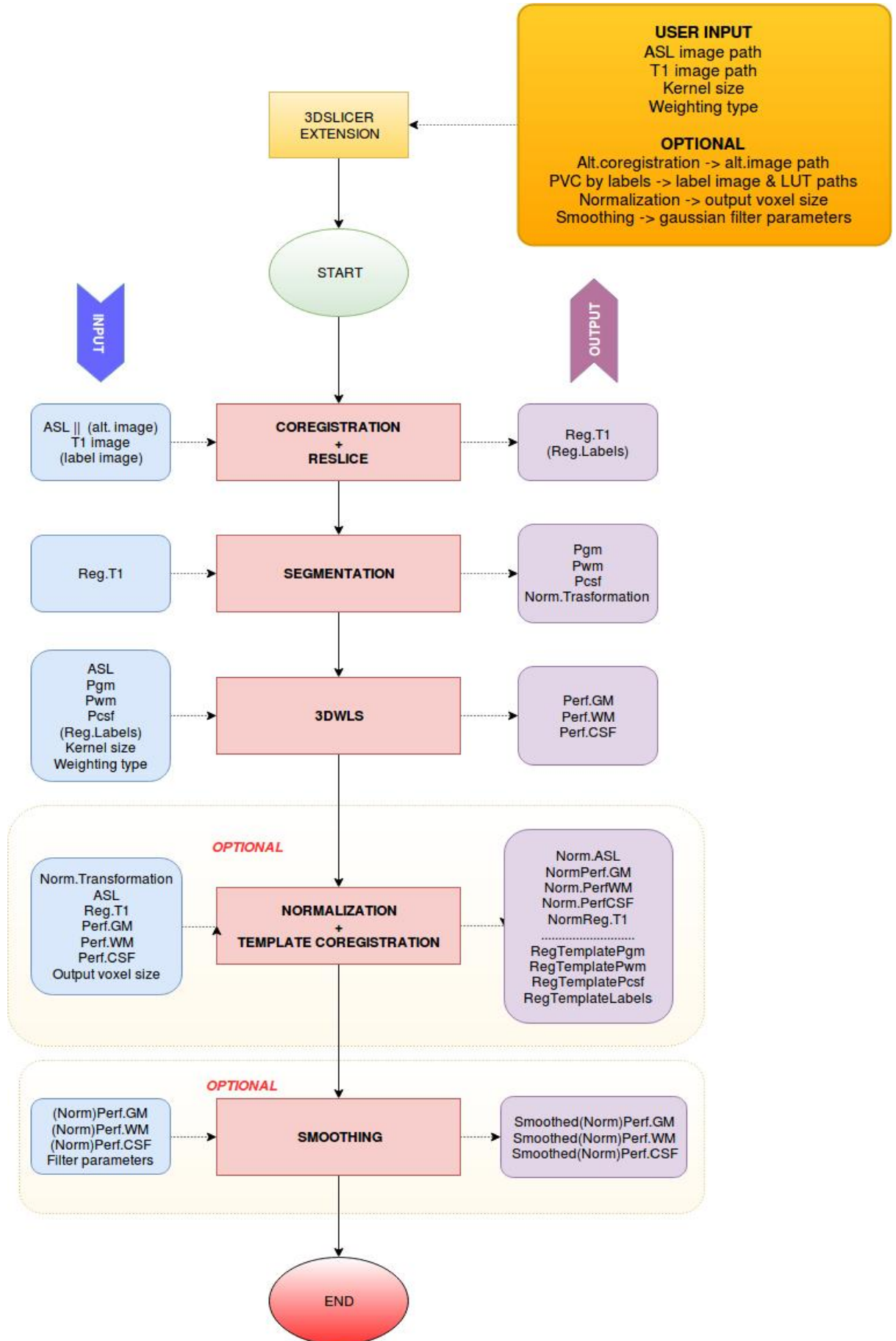
The images of interest resulting from the computation pipeline are loaded into the 3DSlicer scene for their visualization.

The extension exports the following data to the output folder:

- The individual perfusion maps for GM, WM and CSF resulting from PVC.
- The coregistered anatomical T1 image.
- The tissue probability maps resulting from segmentation
- The coregistered label volume, if label option is checked
- The normalized anatomical, segmentation and perfusion maps if the normalization option is checked
- A text data file containing the following information:
 - The paths to the imported files
 - The options and parameters selected by the user
 - Mean GM, WM and CSF intensity values for the whole image; and for each of the regions if label option was checked
 - The date and time at which the job execution was started and finished.

In the text file, the values are separated by single blank spaces and lines so that the information contained in the file is easily importable in calculus sheet software like Microsoft Excel or LibreOffice Calc.

3.3 Extension workflow diagram



CHAPTER 4: Comparison of cerebral perfusion in Alzheimer's disease

The objective of this study is to determine and localize possible cerebral perfusion alterations in Alzheimer's disease compared to normal perfusion patterns, by using ASL MRI.

4.1 Brief overview of Alzheimer's disease

Alzheimer's disease (AD) is a degenerative neurological disorder that produces a progressive decay on the brain function and structure.

While a certain decline in cognition occurs as a natural effect of aging, the dementia associated with the AD is much faster and pronounced. The evolution of the AD is quite well characterized. At early stages of the disease, there is a noticeable decay in short-term memory and learning capacity. As AD progresses, this memory decay becomes more general and acute, and additional gradual cognition deficits appear, including: language problems, mood changes (irritability, aggressiveness) visual recognition and orientation, reasoning and voluntary movements. At the last stage of the disease, there is a general loss in body function which causes the death of the patient. The average life expectancy is 3-10 years [23] depending on the patient's age and the promptness of diagnosis. Nowadays, there is no cure for AD and the therapies are at an early stage of development.

The causes of AD are diverse and currently not well known. At a cellular level, AD shows a progressive loss of cortical neurons in brain areas related to cognitive functions and the synaptic connections within these areas. Recent studies suggest that these neuronal and synaptic losses are caused by accumulation of insoluble beta amyloid proteins. The accumulation is thought to cause an inflammatory response that induces the cellular and synaptic destruction. There are several risk factors that favor the development of the AD: age, genetic predisposition, diabetes, hypertension, obesity, smoking or recurrent head injuries. Among those factors, the most important is age, being the 95% of AD patient 65 years old or more [24].

4.2 Subjects and methods

Subjects

The perfusion study was conducted over the ASL images of 38 subjects in resting conditions: 19 diagnosed AD subjects (mean age = 77, standard deviation = 8) and 19 healthy subjects (mean age = 70, standard deviation = 5).

Image acquisition

The T1 and ASL images were taken by the Group of Dementia of Comunidad de Madrid (DEMCAM) between 2008 and 2011. Images were acquired using a 3T magnetic resonance scanner (SignaHDx 3.0T MR system, GE Healthcare). The ASL acquisition parameters were: TR = 1322 ms, TE= 4.906 ms, flip angle= 155°. The T1 acquisition parameters were: TR = 9.24 ms, TE= 4.152 ms, flip angle= 12°.

Image processing

The perfusion analysis was conducted over the average of all ASL images taken for each subject during acquisition, thus having a mean ASL image for each subject for the perfusion analysis.

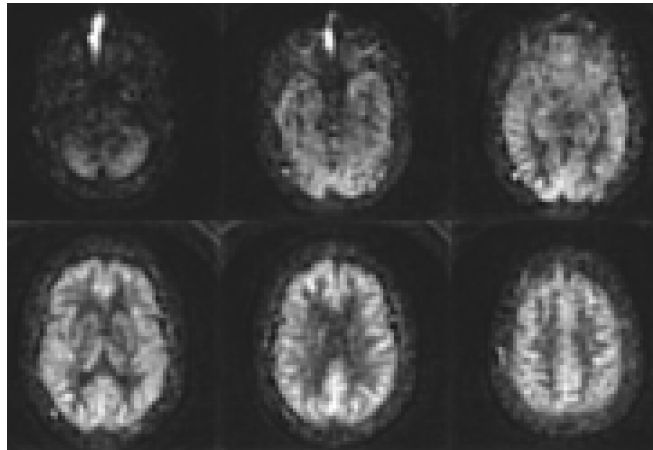


Fig. 4.1 slices from the average ASL image of one subject of the study

The images were PVE corrected (3DWLS) and spatially processed using the 3DSlicer extension described in the previous chapter. The parameters chosen for PVC were an inverse exponential weighting kernel with size 3x3x3 voxels, which was proven the optimal selection of weighting kernel parameters for PVC (as described in chapter 2). Regarding the spatial post-processing, normalization and smoothing over the correction output were enabled to later undergo the group statistical analysis. It was selected a normalization output voxel size of 2x2x4 mm and a smoothing kernel of full width at half maximum (FWHM) equal to 3 times the normalization voxel size, being this kernel width a common standard used in fMRI [25].

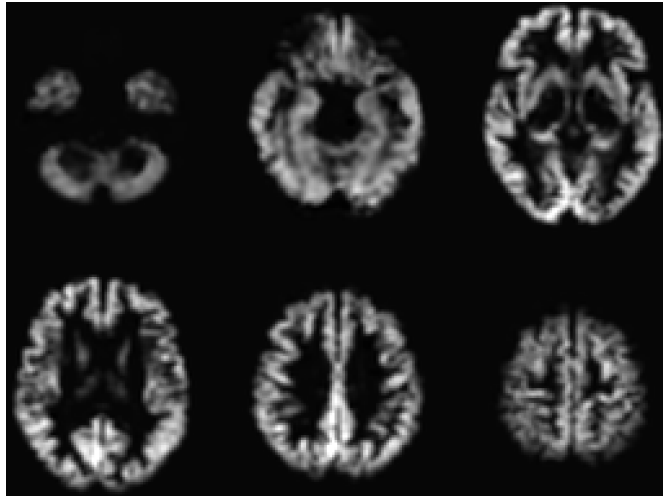


Fig. 4.2 slices from the corrected GM perfusion of one subject of the study

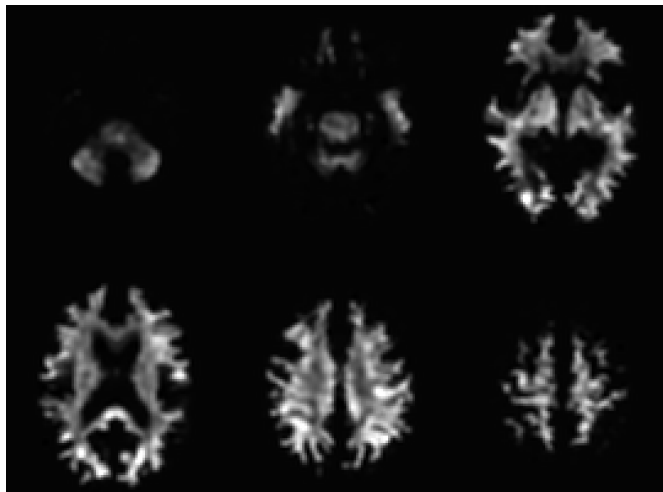


Fig. 4.3 slices from the corrected WM perfusion of one subject of the study

Statistical analysis

A one way analysis of variance (ANOVA) was conducted over the output GM and WM perfusion images independently, to identify significant perfusion differences between the AD and control groups for both brain tissues. The average perfusion in GM and WM for each subject was included as a covariate variable to account for the perfusion variation among different individuals. The statistical analysis was done using the SPM software suite.

4.3 Results and discussion

The next figures show the statistically significant perfusion differences (t values) between AD and control groups, at a P value < 0.005 and with a cluster size > 125 voxels.

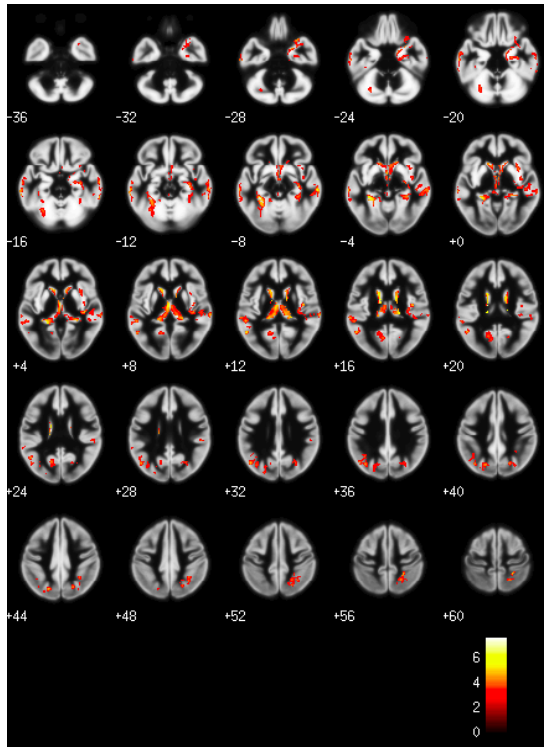


Fig. 4.4 statistic results (Control > Alzheimer), GM perfusion

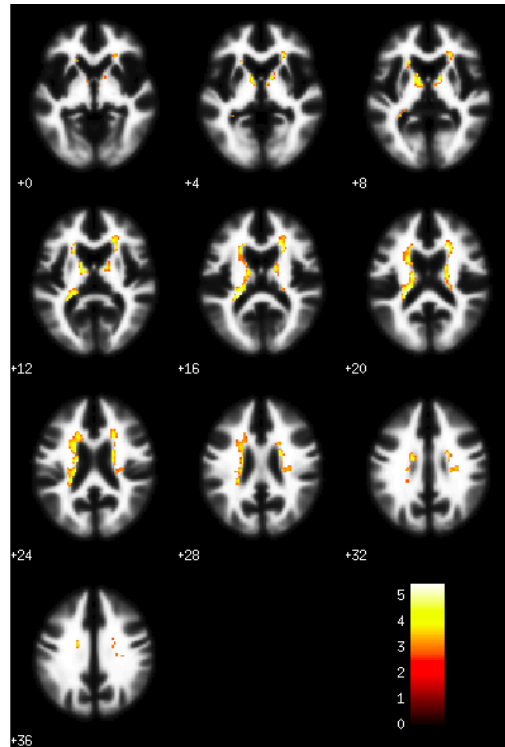


Fig. 4.5 statistic results (Control > Alzheimer), WM perfusion

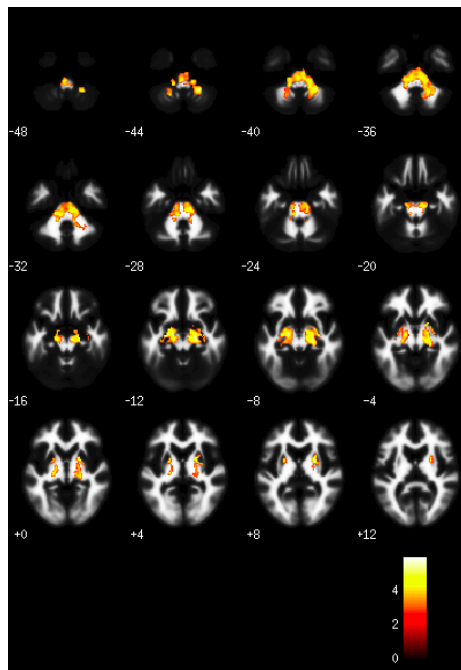


Fig. 4.6 statistic results (Alzheimer > Control), WM perfusion

Significant AD hypoperfusion was found in left and right caudate nucleus and thalamus. Smaller hypoperfusion clusters were also found at the right hippocampus, left and right cuneus and right anterior insula. Additional scattered GM hypoperfusion is present along the middle temporal gyrus and right and left exterior cerebellum. On the other hand, significant AD hyperperfusion was found in the left and right putamen, brain stem and cerebellum white matter. No significant AD hyperperfusion clusters were found in GM.

Several previous studies about AD have reported the presence of anatomical atrophies in the caudate nucleus, thalamus, hippocampus, regions of the temporal lobe, and cuneus [26]. These cerebral regions are closely related with the cognitive impairment associated with the AD:

REGION	T VALUE	FUNCTIONS RELATED TO AD
Caudate nucleus	Left ->4.91 Right ->4.93	Memory, learning, language
Thalamus	Left ->4.58 Right ->4.64	Supports language and motor systems
Hippocampus	Right ->4.2	Memory, spatial orientation
Anterior insula	Right ->3.45	Limbic related functions (basic emotions)
Cuneus	Left ->4.14 Right ->3.05	Self-consciousness, memory, visio-spatial processing
Middletemporal gyrus	Left ->3.85 Right ->4.27	Known faces recognition, written word comprehension
Cerebellum (exterior)	Left ->3.13 Right ->3.86	Motor coordination and precision, motor learning
Cerebellum (white matter)	Left ->-4.61 Right ->-4.00	
Brain stem	-4.03	Nerve impulse conduction, cardiovascular and respiratory system control, awareness and consciousness
Putamen	Left ->-3.80 Right ->-5.27	Motor performance, motor learning

- Positive T values stand for **increased perfusion in control group**. Negative values stand for **increased perfusion in AD**.

The AD hypoperfusion observed in those cerebral regions can be a consequence of the AD-characteristic volume reduction. Regarding the observed AD hyperperfusion, some studies suggest that hyperperfusion in AD serves as a compensatory mechanism. The hypoperfusion found in the cuneus, precuneus, hippocampus and temporal cortex and the hyperperfusion found in the putamen are in agreement with the results reported in other previous studies [27].

Although it is not yet known whether the cerebral hypoperfusion causes the AD or is a consequence of it, the results obtained in the present and other previous studies demonstrate that the perfusion pattern can be a promising biomarker for evaluating AD. ASL has also been demonstrated as a very suitable imaging technique for AD characterization.

Perfusion comparison without PVC

The same perfusion study was also conducted using the normalized original ASL images of the subjects without applying PVC. This was done to check the effects of the correction over analysis.

The results obtained were the following (same P value and cluster size):

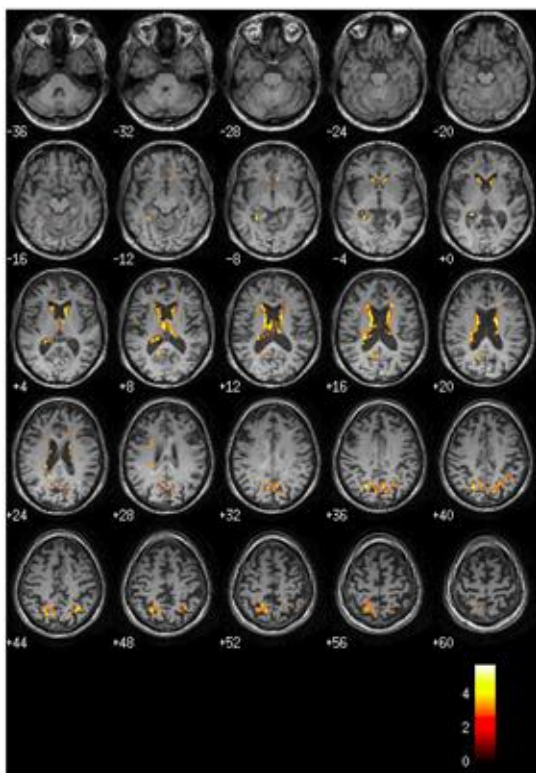


Fig. 4.7 statistic results (Control > Alzheimer), original ASL

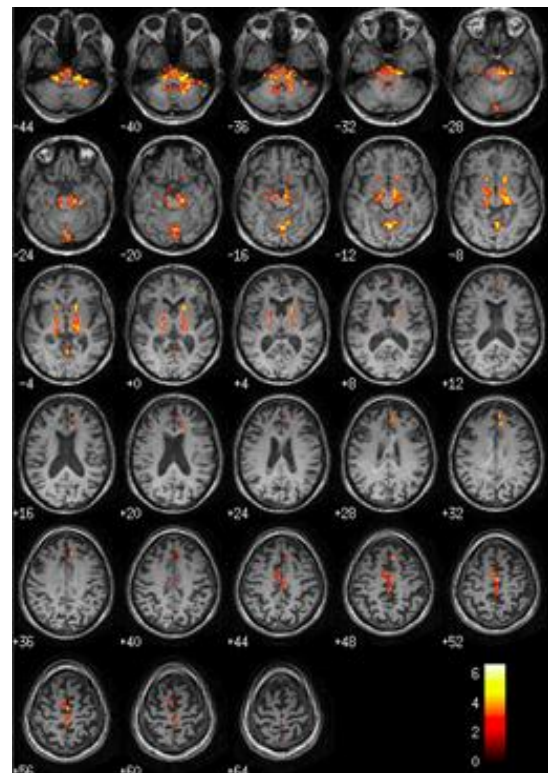


Fig. 4.8 statistic results (Alzheimer > Control), original ASL

Control hyperperfusion is still clear at the caudate nucleus, the thalamus and the cuneus. A small hyperperfusion cluster is also found at the left hippocampus, which was not the case for the corrected images, and in the right anterior insula. For the other regions though, control hyperperfusion pattern disappears with respect the corrected images. AD hyperperfusion is still present at the brain stem, putamen and the exterior cerebellum. Unlike the corrected case, no AD hyperperfusion was present in the cerebellar white matter.

In general, the statistical significance values (T values) in the clusters are lower and less uniform for the uncorrected case. The following table contains the T values for the uncorrected case taken at the exact same previous locations:

REGION	T VALUE
Caudate nucleus	Left ->4.41
	Right ->3.65
Thalamus	Left ->4.38
	Right ->3.59
Hippocampus	Left ->4.25
	Right ->1.66
Anterior insula	Right ->3.49
Cuneus	Left ->0 (some scattered low hyperperfusion)
	Right ->0 (some scattered low hyperperfusion)
Middletemporal gyrus	NO HYPERPERFUSION
Cerebellum (exterior)	Left ->3.79
	Right ->1.99
Cerebellum (white matter)	Left ->-2.90
	Right ->-5.33
Brain stem	0 (some scattered AD hyperperfusion)
Putamen	Left ->-1.39
	Right ->-2.22

- Positive T values stand for **increased perfusion in control group**. Negative values stand for **increased perfusion in AD**.

CONCLUSION AND FUTURE WORK

The **main objectives** of this bachelor thesis were: (1) **develop and evaluate a new algorithm for PVC of ASL images**, (2) **integrate this algorithm into a 3DSlicer GUI extension** that automates the standard image processing workflow and (3) **validate the algorithm and extension by conducting a real comparative perfusion study** between AD and control.

Based on the previous state-of-the-art method for PVC developed by Asllani et Al, the proposed **3DWLS algorithm enhances the mentioned method** by substituting the 2D correction by a **3D correction and introducing a weighting** to the least squares problem as a function of the distance, which better satisfies the perfusion uniformity assumption around the central voxel.

The **3DWLS algorithm was evaluated using artificial general CBF images** constructed from the addition of simulated GM, WM and CSF perfusion images. The evaluation consisted in applying the PVC to the general CBF images and then **measuring the RMSE between the correction results and the original simulated individual perfusion maps**. Different combinations of parameters (regression kernel size and weighting type) were tested to find the optimal one giving the lowest error. The **optimal combination of parameters** was found to be an **inverse exponential of the distance weighting** with a **regression kernel size of 3x3x3 voxels**. Another weighting as a function of the voxel tissue heterogeneity was explored but it had no improvement in terms of RMSE value. A correction by the **Asllani's algorithm was also included in the evaluation** process for comparison against the 3DWLS. Regardless of the 3DWLS weighting type selected, the **3DWLS gave significantly lower RMSE values than the Asllani's algorithm**. When choosing the mentioned optimal parameters for the 3DWLS, the total RMSE error was $\approx 52.2\%$ lower; the GM RMSE error was $\approx 29.7\%$ lower and the WM RMSE was $\approx 5.5\%$ lower compared to Asllani's algorithm.

The **3DSlicer extension** is a **useful tool for researchers** needing to perform PVC of ASL images in their studies. The **user interface is simple and clear**, allowing the user to easily select the desired parameters and **carry out the complete image correction process, following the usual standards** of functional neuroimaging processing. The extension **automates the spatial preprocessing** of the input images (coregistration, segmentation), the **3DWLS execution** and the **spatial postprocessing** (normalization, smoothing) of the PVC output.

Both the 3DWLS and the extension were used successfully to correct perfusion images from AD and control subjects, in order to **carry out a real comparative perfusion study**. **AD hypoperfusion regions were found**, among others, in the **thalamus, caudate nucleus, hippocampus and cuneus**. These **findings are in agreement with previous reported perfusion studies** and are **consistent with the expected affected regions in**

AD as they are related with memory, spatial orientation, learning and language cognitive functions. Besides from the scientific interest of the results, this provides further validation of both the 3DWLS and the extension for conducting neuroimaging studies.

Some **future work lines** to be explored are:

- **Further evaluation of the 3DWLS algorithm over real MRI images.** Computer-generated CBF maps provide a straightforward but simplistic approach for testing the algorithm. A more trusty evaluation approach could be through ASL images taken from an MR phantom, in which individual tissue perfusion could be precisely simulated and controlled.
- The **3DSlicer extension**, although fully functional, is still at development stage and **should be debugged for improving computing efficiency**. Currently, the extension is only compatible with Linux-based systems and requires manual compilation from the python source code and manual installation of the dependencies to work. **Adaptation to other system platforms and automatic installation of the extension and dependencies is still pending.** **Additional functionalities** are also being considered, like importation and correction of multiple image files (at the moment, PVC must be done for one ASL image at a time) and including the statistical group analysis in the extension workflow.

SOCIO-ECONOMIC FRAMEWORK

By year 2015, it was estimated that 46.8 million people were suffering from dementia, being the AD the most common cause of irreversible dementia (~70%). The number of affected people is expected to double every 20 years, due to the progressive aging of the global population. The worldwide prevalence of dementia supposed a global healthcare cost of US\$ 818 billion in 2015. This cost, as the dementia prevalence, has also a growing trend [28].

This high economic burden, together with the notorious impact that AD (and dementia in general) has over the patients and their relatives, has raised a great research interest and effort to clarify the causes of AD and discover new diagnostic and treatment methods.

The algorithm for PVC presented in this work provides a more accurate correction of ASL imaging than the previous existing methods. This could be useful for obtaining better characterization and diagnostic methods for AD through ASL in the future. This, in turn, will have a positive impact in treatment planning and cost reduction.

The GUI extension developed in this work automates and speeds up the image processing step, which allows the researchers saving the work time that would be otherwise expended in this routine process. This indirectly has a positive cost impact in their research projects.

- **Project budget**

The time invested in this project was 5 months (20 hours/week), excluding the project document writing period.

HUMAN COST	Cost (€/hour)	Dedicated hours	Total cost (€)
Tutorship	15	40	600
Student	-	400	-

MATERIAL COST	Cost (€)	Total cost (€)
Image acquisition	500 (per subject)	19,000
MATLAB	500 (academic license)*	58.33
	200 (image processing toolbox)*	
Personal computer	600*	50

TOTAL PROJECT COST (€)	19708.33
-------------------------------	-----------------

*Assuming an amortization of 100% at 5 years for the software and the computer

REGULATORY FRAMEWORK

- **Software licensing**

3DSlicer platform is an open source software distributed under a BSD-style license [29][30] which grants “no restrictions on use of the software”, allowing the free download, copy, modification and redistribution of the software under agreement of its license terms.

CTK library is open source and licensed under Apache v2.0 [31], allowing users to use the code for any purpose freely and without distribution restrictions [32].

Qt library is open source and relies on a triple licensing system [33]: GNU LGPL (free, intended for commercial applications), GNU GPL (free, intended for open source and free software development) and a QPL proprietary license. The license applying to this project is the GPL license [34] which grants the copy, modification and redistribution of the software and forces the new software and source code to be freely distributed under the same license.

SPM suite is free and open source software licensed [35] under the terms of the GNU GPL v.2.

The 3DSlicer extension developed during this project is also licensed under the terms of the GNU GPL license, being the code currently available upon request. The use, copy, modification and distribution of the software are allowed, under the copyleft requirements. The software has been developed for research purposes only, and has not been revised or approved by any competent agency. The developer and contributors disclaim all warranties of any kind, assuming the user all possible liability derived from its use.

- **Study subjects**

All the subjects of the study were properly informed about the imaging procedure via an exhaustive written form. Through this form, past clinical procedures were assessed together with the presence of possible implants or objects that could imply a potential safety threat for the subjects during the scanning process.

The subjects were also given a proper informed consent form, in which they stated to have read and understand the safety instructions and voluntarily agreed to the MRI examination and the use of this images for scientific publications or investigation projects.

Bibliography

- [1] Alsop, D.C., Dai, W., Grossman, M., Detre, J. A. (2010). *Arterial Spin Labeling Blood Flow MRI: Its Role in the Early Characterization of Alzheimer's Disease*. Journal of Alzheimer's Disease : JAD, 20(3), 871–880 <http://doi.org/10.3233/JAD-2010-091699>
- [2] Parkes, L. M., Rashid, W., Chard, D. T. and Tofts, P. S. (2004), *Normal cerebral perfusion measurements using arterial spin labeling: Reproducibility, stability, and age and gender effects*. Magn. Reson. Med., 51: 736–743. <http://doi.org/10.1002/mrm.20023>
- [3] Schild, H.H. (1990). *MRI made easy (...well almost)*. Berlin: Schering. ISBN: 3921817412
- [4] Driggers, R.G. (2003). *Encyclopedia of Optical Engineering: Las-Pho*. Vol. 2. 1025-2048. CRC Press. ISBN: 0824742516
- [5] Hornak, J.P. (1996). *The Basics of MRI*. Rochester, NY: Rochester Institute of Technology. <https://www.cis.rit.edu/htbooks/mri/inside.htm>
- [6] Hashemi, R., Bradley, W.G., Lisanti, C.J. (2010) *MRI, the Basics*. LWW. ISBN: 1608311155
- [7] Chavhan, G. B., Babyn, P. S., Thomas, B., Shroff, M. M., & Haacke, E. M. (2009). *Principles, Techniques, and Applications of T2*-based MR Imaging and Its Special Applications*. Radiographics, 29(5), 1433–1449. <http://doi.org/10.1148/rg.295095034>
- [8] McRobbie, D.W. (2003) *MRI from Picture to Proton*. Cambridge University Press. ISBN: 0521523192
- [9] Bernstein, M.A., King, K.F., Zhou, X.J. (2004) *Handbook of MRI Pulse Sequences*. Elsevier. ISBN: 0080533124
- [10] Poustchi-Amin, M., Mirowitz, S.A., Brown, J.J., McKinstry, R.C., Li, T. (2001) *Principles and Applications of Echo-Planar Imaging: a Review for the General Radiologist*. Radiographics, 21(3), 767-779
- [11] Imaging Equipment Sales Prices. Offers.blockimaging.com. Retrieved 17 February 2017, from <https://offers.blockimaging.com/imaging-equipment-sales-prices>
- [12] Kudomi, N., Maeda, Y., Sasakawa, Y., Monden, T., Yamamoto, Y., Kawai, N., Nishiyama, Y. (2013). *Imaging of the appearance time of cerebral blood using [¹⁵O] H₂O PET for the computation of correct CBF*. EJNMMI Research, 3, 41. <http://doi.org/10.1186/2191-219X-3-41>
- [13] Maton, A, Hopkins, J, McLaughlin, C.W., Johnson, S., Warner, M.Q., LaHart, D., Wright, J.D. *Human Biology and Health*. (1993) Englewood Cliffs, New Jersey, USA: Prentice Hall. ISBN: 0139811761
- [14] Djamali, A., Sadowski, E.A., Muehrer, R.J., Reese, S., Smavatkul, C., Vidyasagar, A., Fain, S.B., Lipscomb, R.C., Hullett, D.H., Samaniego-Picota, M., Grist, T.M., Becker, B.N. (2007) *BOLD-MRI assessment of intrarenal oxygenation and oxidative stress in patients with chronic kidney allograft dysfunction*. American Journal of Physiology. Renal Physiology 292(2) F513-22 DOI: 10.1152/ajprenal.00222.2006
- [15] Alsop, D. C., Detre, J. A., Golay, X., Günther, M., Hendrikse, J., Hernandez-Garcia, L., ...Zaharchuk, G. (2015). *Recommended Implementation of Arterial Spin Labeled Perfusion MRI for Clinical Applications: A consensus of the ISMRM Perfusion Study Group and the European Consortium for ASL in Dementia*. Magnetic Resonance in Medicine, 73(1), 102–116. <http://doi.org/10.1002/mrm.25197>

- [16] Pollock, J. M., Tan, H., Kraft, R. A., Whitlow, C. T., Burdette, J. H., & Maldjian, J. A. (2009). *Arterial Spin Labeled MRI Perfusion Imaging: Clinical Applications*. *Magnetic Resonance Imaging Clinics of North America*, 17(2), 315–338. <http://doi.org/10.1016/j.mric.2009.01.008>
- [17] Golay, X., Petersen, E. T. and Hui, F. (2005), Pulsed star labeling of arterial regions (PULSAR): A robust regional perfusion technique for high field imaging. *Magn. Reson. Med.*, 53: 15–21. <http://doi.org/10.1002/mrm.20338>
- [18] Aguirre, G.K. Detre, , J.A., Zarahn, E. , Alsop, D.C. (2002) *Experimental Design and the Relative Sensitivity of BOLD and Perfusion fMRI*, *NeuroImage*, Vol. 15. (3). 488-500, <http://dx.doi.org/10.1006/nimg.2001.0990>
- [19] Johnson, N. A., Jahng, G.-H., Weiner, M. W., Miller, B. L., Chui, H. C., Jagust, W. J., ... Schuff, N. (2005). *Pattern of Cerebral Hypoperfusion in Alzheimer Disease and Mild Cognitive Impairment Measured with Arterial Spin-labeling MR Imaging: Initial Experience*. *Radiology*, 234(3), 851–859. <http://doi.org/10.1148/radiol.2343040197>
- [20] Asllani, I., Borogovac, A., Brown, T. R. (2008), *Regression algorithm correcting for partial volume effects in arterial spin labeling MRI*. *Magn. Reson. Med.*, 60: 1362–1371. <http://doi.org/10.1002/mrm.21670>
- [21] Garcia-Polo, P., Martín, A., Mato, V., Quirós, A., Zelaya, F., Hernández-Tamames, J.A. (2015) *3D Weighted Least Squares Algorithm for Partial Volume Effect Correction in ASL Image*. Toronto: ISMRM 2015
- [22] Fedorov A., Beichel R., Kalpathy-Cramer J., Finet J., Fillion-Robin J.-C., Pujol S., Bauer C., Jennings D., Fennessy F.M., Sonka M., Buatti J., Aylward S.R., Miller J.V., Pieper S., Kikinis R. (2012) *3D Slicer as an Image Computing Platform for the Quantitative Imaging Network*. *Magn Reson Imaging*. 30(9):1323-41. PMID: 22770690. PMCID: PMC3466397. <https://www.slicer.org>
- [23] Zanetti O, Solerte S.B, Cantoni F. (2009) Life expectancy in alzheimer's disease. *Arch Gerontol Geriatr*. 49:237–243. <http://doi.org/10.1016/j.archger.2009.09.035>
- [24] Korolev, I.O. (2014) *Alzheimer's Disease: A Clinical and Basic Science Review*. *Medical Student Research Journal*, (4) 24-33.
- [25] Lindquist, M. (2008). *The Statistical Analysis of fMRI Data*. *Statistical Science*, 23(4), 439-464
- [26] Austin, B. P., Nair, V. A., Meier, T. B., Xu, G., Rowley, H. A., Carlsson, C. M., Prabhakaran, V. (2011). *Effects of Hypoperfusion in Alzheimer's Disease*. *Journal of Alzheimer's Disease*, 26(Suppl 3), 123–133. <http://doi.org/10.3233/JAD-2011-0010>
- [27] Wolk, D. A., & Detre, J. A. (2012). *Arterial Spin Labeling MRI: An Emerging Biomarker for Alzheimer's Disease and Other Neurodegenerative Conditions*. *Current Opinion in Neurology*, 25(4), 421–428. <http://doi.org/10.1097/WCO.0b013e328354ff0a>
- [28] Prince, M., Wimo, A., Guerchet, M., Ali, G.C. , Wu, Y.T., Prina, M. (2015) *World Alzheimer Report 2015: The Global Impact of Dementia. An Analysis of Prevalence, Incidence, Cost and Trends*. London: Alzheimer's Disease International (ADI)
- [29] The FreeBSD Copyright.. [Freebsd.org.. Retrieved 17 February 2017, from https://www.freebsd.org/copyright/freebsd-license.html](https://www.freebsd.org/copyright/freebsd-license.html)
- [30] License - SlicerWiki. [Slicer.org. Retrieved 17 February 2017, from https://www.slicer.org/wiki/License](https://www.slicer.org/wiki/License)

- [31]Apache License, Version 2. (2017). Apache.org. Retrieved 17 February 2017, from <http://www.apache.org/licenses/LICENSE-2.0>
- [32]CommonTk. CommonTk.org Retrieved 17 February 2017, from http://commonTk.org/index.php/Main_Page
- [33]Qt-Legal | Licensing. Qt. Retrieved 17 February 2017, from <https://www.qt.io/licensing>
- [34]What is Copyleft? - GNU Project - Free Software Foundation. (2017). Gnu.org. Retrieved 17 February 2017, from <http://www.gnu.org/copyleft>
- [35]NeuroImaging, W. SPM software - Statistical Parametric Mapping. Fil.ion.ucl.ac.uk. Retrieved 17 February 2017, from <http://www.fil.ion.ucl.ac.uk/spm/software>

- **VISUAL RESOURCES**

- [36]Thomas, G. *Nucleus Magnetic Resonance (NMR)*. 2016. Web: <http://brussels-scientific.com/?p=6273> 8 Dec. 2016
- [37]Brigham Young University. *Alignment in Magnetic Fields*. Web: http://bio.groups.et.byu.net/mri_training_b_Alignment_in_Magnetic_Fields.phtml 14 Feb. 2017.
- [38]Puddephat, M. *The Principles of Magnetic Resonance Imaging*. Web: <http://www.voxelcube.com/articles/1/the-principles-of-magnetic-resonance-imaging> 14 Feb. 2017.
- [39]Kleinnijenhuis, M. PhD Thesis (2014) *Imaging fibres in the brain*. Pag. 48 ISBN: 9789491027994
- [40]Gibby, W.A. *Basic principles of magnetic resonance imaging*. (2005) Neurosurgery Clinics of North America , Vol. 16 , Issue 1 , 1 – 64 ISSN 10423680 <http://dx.doi.org/10.1016/j.nec.2004.08.017>
- [41]Heggie, J.C.P., Liddell, N. A., Maher, K.P. *Applied Imaging Technology* (2001). Melbourne: St Vincent's Hospital. 1-490. ISBN 1875271333
- [42]MRI Questions & Answers; *MR Imaging Physics & Technology. Questions and Answers in MRI*. Web: http://mriquestions.com/uploads/3/4/5/7/34572113/_1006945_orig.gif 15 Dec. 2016.